inorganics

MDPI

Review

Bridgman Method for Growing Metal Halide Single Crystals: A Review

Hui Zhu [1,†], Suqin Wang [1,†], Ming Sheng [1], Bo Shao [1], Yu He [1], Zhuang Liu [2,*] and Guangtao Zhou [1,*]

[1] College of Engineering, Shandong Xiehe University, Jinan 250109, China; zhuhui@sdxiehe.edu.cn (H.Z.); wangsuqin@sdxiehe.edu.cn (S.W.); shengming@sdxiehe.edu.cn (M.S.); shaobo@sdxiehe.edu.cn (B.S.); heyu@sdxiehe.edu.cn (Y.H.)
[2] School of Materials Science and Engineering, Shandong University, Jinan 250061, China
* Correspondence: liu.zhuang@sdu.edu.cn (Z.L.); charlie@sdxiehe.edu.cn (G.Z.)
† These authors contributed equally to this work.

Abstract: The Bridgman method for single-crystal growth enables the formation of crystals at the lower end of the molten material by cooling it under a precisely controlled temperature gradient. This makes it particularly suitable for producing high-quality single-crystal materials. Over the years, the Bridgman technique has become widely adopted for growing single crystals of semiconductors, oxides, sulfides, fluorides, as well as various optoelectronic, magnetic, and piezoelectric materials. Recently, there has been growing interest in metal halide materials, with the growth of high-quality metal halide single crystals emerging as a major focus for both the scientific community and industry. However, traditional solution-based single-crystal growth methods have several limitations, such as slow growth rates, inconsistent crystal quality, challenges in solvent selection, and difficulties in controlling saturation levels. These issues present significant obstacles, particularly when large, defect-free, high-quality single crystals are needed for certain high-performance materials. As a result, the Bridgman method has emerged as an effective solution to overcome these challenges. This review provides an overview of various categories of metal halide single-crystal systems grown using the Bridgman method in recent years. The systems are classified based on their dimensionality into three-dimensional, two-dimensional, and zero-dimensional metal halide structures. Furthermore, we highlight novel metal halide single crystals developed through the Bridgman technique. Additionally, we offer a brief introduction to the structures, properties, and applications of these single crystals, underscoring the crucial role of the Bridgman method in advancing research in this field.

Keywords: metal halide; single crystal; Bridgman method; photoelectric properties; applications

check for updates

Academic Editors: Sake Wang, Nguyen Tuan Hung and Minglei Sun

Received: 9 January 2025
Revised: 7 February 2025
Accepted: 10 February 2025
Published: 11 February 2025

Citation: Zhu, H.; Wang, S.; Sheng, M.; Shao, B.; He, Y.; Liu, Z.; Zhou, G. Bridgman Method for Growing Metal Halide Single Crystals: A Review. *Inorganics* **2025**, *13*, 53. https://doi.org/10.3390/inorganics13020053

Copyright: © 2025 by the authors. Licensee MDPI, Basel, Switzerland. This article is an open access article distributed under the terms and conditions of the Creative Commons Attribution (CC BY) license (https://creativecommons.org/licenses/by/4.0/).

1. Introduction

The Bridgman method for single-crystal growth is a pivotal technique, which has been extensively utilized in the preparation of single crystals for semiconductor materials, optoelectronic devices, and other high-performance materials [1–3]. First proposed by the American scientist Theodore Bridgman in 1915, it has since evolved into one of the most established technologies for producing single crystals with high quality [4]. The Bridgman method is renowned for its process stability, precise controllability, and stringent material requirements, making it a fundamental technique in materials science, particularly in research focused on high-purity and high-quality single crystals [5–7].

1.1. Basic Principle

As illustrated in Figure 1a, the Bridgman method operates on the principle of the dissolution-crystallization process [8–11]. Through controlling the temperature gradient precisely, the material within the solution gradually cools, facilitating the transition from the liquid solution to solid state, thereby yielding a single crystal. In this process, the material is first heated above its melting point to form a liquid phase, and then it is progressively cooled under a controlled temperature gradient, promoting the crystallization of the material from liquid state to solid status [12,13]. The Bridgman method is particularly effective for materials with high melting points that can maintain stability at elevated temperatures, such as certain semiconductor materials, ceramics, and metal alloys [14].

It should be noted that there are necessary ways to determine the appropriate method in advance for growing different halide single crystals. In other words, not all halide single crystals can be grown using the Bridgman method. Although a large body of previous work suggests that potential halides can be predicted using simulation methods, growing these potential halide single crystals faces significant uncertainty [15,16]. A phase diagram is a concise graphical representation of the relationship between the components, temperature, and pressure of a system at thermodynamic equilibrium. Initially, phase diagrams were obtained through extensive experiments [17]. With the development of computational materials science, computational phase diagrams based on molecular dynamics have become an efficient method for obtaining phase diagrams [18–20]. For halides, by referencing phase diagrams of related components, it is possible to determine whether the single crystal of the compound is likely to grow easily [21]. Taking the binary phase diagram of chlorides as an example, a large number of previous works have summarized the synthesis conditions of approximately one thousand halides, including their melting points, whether they fully crystallize, lattice structures, and space groups [22]. In the relevant literature, researchers have even been able to compile statistics on how many reported works have successfully grown halide single crystals and the preparation methods they used. In the future, as more and more new halides are successfully synthesized, these phase diagrams will continue to expand, becoming a reference handbook for researchers. It should be noted that, compared to solution-based crystal growth, the progress of phase diagrams in this field will be slower because methods for growing large single crystals, such as the Bridgman method, require more expensive and larger-scale growth equipment, which is not always available for researchers.

1.2. Experimental Setup for the Bridgman Method

As exhibited in Figure 1b, the experimental setup for the Bridgman method comprises several essential components: a high-temperature furnace, a crucible, a cooling system, and a temperature gradient control system [8,23]. The high-temperature furnace is used to heat the crucible and create a high-temperature environment for the process. The furnace's temperature control system allows for precise regulation of the heating temperature and distribution, ensuring uniform heating and melting of the material [24]. The crucible serves as the container for the material to be crystallized and is typically constructed from high-temperature-resistant materials such as quartz or platinum [25]. The selection of the crucible material must account for both chemical stability and resistance to high temperatures. The Bridgman method relies on a cooling process to guide the material from liquid phase to a solid state [26]. Therefore, a cooling system is essential to facilitate this phase of the process. Water or air cooling systems are commonly employed to regulate the cooling rate. During this process, precise control over the temperature gradient is critical. The temperature gradient is a key factor influencing the success of the Bridgman method [27]. By controlling the temperature range of the furnace and the cooling system, a

suitable temperature gradient can be maintained from the top to the bottom of the crucible, thereby promoting the preparation of high-quality single crystals.

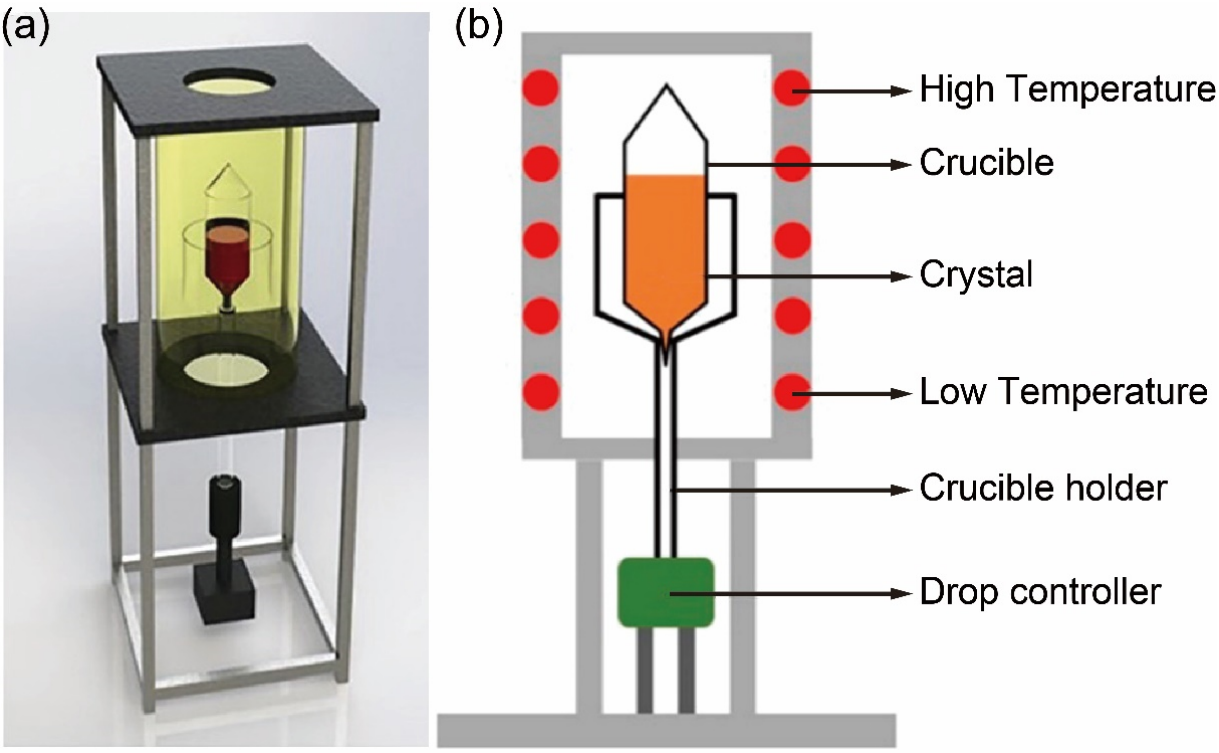


Figure 1. (**a**) Three-dimensional diagram of a typical Bridgman furnace. Reprinted with permission from Ref. [8]. Copyright 2021, Royal Society of Chemistry. (**b**) Planar graph of vertical Bridgman furnace and their key assemblies. Reprinted with permission from Ref. [23]. Copyright 2018, American Chemical Society.

1.3. Growth Process

The growth process using the Bridgman method for single crystals is typically divided into several stages. First, the raw materials intended for crystal growth are placed in the crucible and heated above their melting point to ensure complete transition into the liquid phase. During the melting process, it is crucial to maintain a stable temperature to prevent excessive bubble formation or the introduction of undesirable impurities [28]. Once the material has fully melted, the next step involves establishing a reasonable temperature gradient by adjusting the high/low-temperature zone. This gradient is achieved by gradually moving the crucible from the high-temperature zone to the lower-temperature zone [29]. Generally, the temperature at the bottom zone is lower, while the top remains hotter. This temperature differential prompts the material to begin crystallizing at the bottom of the crucible, initiating the growth of single crystals. As the temperature decreases, the material transitions from a liquid state to a solid phase. Under the influence of the temperature gradient, crystal nuclei begin to form in the lower-temperature region of the crucible. As the solution becomes supersaturated, crystals start to deposit on the liquid's surface. The process must proceed slowly to ensure smooth crystal growth and the formation of a single, high-quality crystal [30]. Over time, the crystal grows steadily out of the liquid and increases in size. When the crystal reaches the desired size, mechanical methods are employed to extract it from the crucible. To minimize the risk of damaging the crystal during removal, the temperature is typically lowered gradually to room temperature, and protective measures are implemented [31]. After extraction, further processing, such as

cutting and polishing, is often conducted to achieve the certain shape and surface quality of the crystal [32].

1.4. Advantages of the Bridgman Method

The Bridgman method, as a traditional technique for single-crystal growth, offers several distinct advantages. First and foremost, it provides precise control over the temperature gradient, a critical factor in achieving high-quality single crystals [33]. The accuracy of temperature regulation directly impacts the quality of as-prepared crystals, making this feature particularly significant. Additionally, the Bridgman method is versatile, suitable for single-crystal growth from wide ranges of materials, including metals, semiconductors, ceramics, and more [34,35]. It is especially advantageous for growing materials with high melting points. Moreover, as the Bridgman method involves a transition from liquid state to solid phase, impurities in the liquid solution are effectively excluded, resulting in single crystals with high purity [36].

The Czochralski method, as another popular technology for single crystal growth, has often been compared to Bridgman method [37]. The Czochralski method is widely used in semiconductor materials and the single crystal growth of high-tech industries such as silicon and germanium [38]. Its advantages include higher growth rate, that the Czochralski method stretches the crystal while it is in a molten state, which results in a relatively fast growth rate, making it suitable for large-scale production [39]. Moreover, since the crystal is gradually stretched in a molten state, more uniform crystals with higher purity can be obtained. In addition, this method is capable of growing large single crystals, suitable for industrial production [40]. However, the Czochralski method has several disadvantages. For example, the equipment for this method is more complex and requires precise control of temperature, stretching rate, and other parameters, thus making it more expensive. In addition, since the crystal is grown by stretching, the process may introduce more defects, especially when not operating under suitable conditions [41].

In summary, the Bridgman method is suitable for high-melting-point materials and precision-demanding applications, but it has a slower growth rate, limited crystal size, and lower cost. The Czochralski method is better suited for large-scale production and single crystals with high purity and uniformity, but the equipment is more complex, costly, and has a limited range of applicability.

1.5. Current Mainstream Applications

The Bridgman method is extensively utilized for synthesis of single crystals for semiconductor materials, ceramics, and corresponding optoelectronic devices [34,35,42]. In the semiconductor industry, for instance, the Bridgman method is employed to grow high-quality single crystals such as gallium arsenide (GaAs), indium phosphide (InP), and other compounds [43,44]. The aforementioned materials are widely applied in fields such as integrated circuits, laser diodes, and solar cells. Additionally, the Bridgman method plays a crucial role in the research and development of high-temperature superconducting materials, ferroelectric materials, and other advanced materials [45–49].

Metal halide materials have garnered considerable attention due to their outstanding photoelectronic properties, particularly their promising potentials in photovoltaics, photocatalysis, and light-emitting devices [15,16,50,51]. For example, all-inorganic perovskite nanocrystal $CsPbBr_3$ has been used as scintillators to provide convenient visualization tool for X-ray radiography [52]. In addition, recent studies indicate that $CsPbBr_3$ nanocrystals can also be applied in quantum computing and quantum communications owing to their excellent single-photon feature when assembled to be superlattice [51]. Metal halides with lower dimensions possess unique properties. For example, zero-dimensional Cs_2MoCl_6

and Cs_2WCl_6 single crystals emit near-infrared light, which can be used in safety inspection and night vision [53]. Low-dimensional organic–inorganic hybrid metal halides as subgroup halide compounds have been widely used in optoelectronic domains. For example, one-dimensional $(C_5H_{11}N_3)MnCl_2Br_2 \cdot H_2O$ exhibited water-molecule-induced reversible photoluminescence transformation, which has been used in anti-counterfeiting field [54].

Metal halide materials are characterized by high melting points and a strong sensitivity to impurities, which means that the single-crystal growth process demands precise control over factors including temperature, liquid concentration, and cooling speed [55–58]. The Bridgman method operates by gradually cooling the material under a controlled temperature gradient, facilitating the transition from liquid state to solid phase. This method allows for effective regulation of both the crystal growth rate and its quality. Moreover, the crystal quality and growth rate of metal halide single crystals are closely dependent on the temperature gradient [59]. The Bridgman method excels in providing a uniform and stable temperature gradient throughout the growth process, making its temperature control capabilities essential for producing high-quality single crystals. Additionally, the cooling process inherent in the Bridgman method effectively excludes impurities, ensuring the formation of high-purity crystals. The removal of impurities is crucial for enhancing the optoelectronic performance of metal halide materials [60]. Furthermore, given the high melting points of many metal halide materials, the Bridgman method's capacity to operate at elevated temperatures makes it particularly well-suited for growing perovskite materials, which require high-temperature conditions [61].

2. Bridgman Method for Growing Three-Dimensional Metal Halide Single Crystals

Three-dimensional (3D) metal halides represent the largest subgroup of metal halides, distinguished by their unique crystal structures and exceptional optoelectronic properties [62–66]. In recent years, they have attracted widespread attention in fields such as optoelectronic devices, photovoltaics, photocatalysis, and light-emitting diodes (LEDs) [67,68]. Three-dimensional metal halides are known for their excellent light absorption properties, including broad absorption spectra and efficient absorption cross-sections, which make them highly effective in energy conversion applications, particularly in photovoltaic devices [69,70]. Notably, in solar cells, 3D metal halides can achieve high energy conversion efficiencies even under low light intensities, positioning them as a key area of research in solar energy. In addition to their optical properties, 3D metal halides exhibit large carrier mobility and excellent carrier diffusion, which makes them highly efficient for use in electronic devices [71–73].

However, 3D metal halides are easily to be degraded when exposed to water and oxygen, which can significantly impair their optoelectronic performance [74,75]. As a result, enhancing the environmental stability and longevity of these materials has become a major focus of ongoing research. Fortunately, large-sized 3D metal halide single crystals prepared by the Bridgman method have demonstrated significantly improved stability [76–78]. Research in this area has experienced rapid growth in recent years, offering promising prospects for addressing these challenges.

Three-dimensional metal halides often undergo nondestructive phase transitions at relatively low temperatures [79]. Taking $CsPbBr_3$ as an example, as shown in Figure 2a, the first phase transition occurs around 403 K, where the material shifts from the cubic phase to tetragonal configuration, with the feature of first-order phase transition. After that, a second-order transition occurs at 361 K to the orthorhombic phase, which finally becomes stable at room temperature [80]. However, residual stress still exists after these transitions, which can induce mechanical deformation and crack formation. Such imperfections can

significantly degrade the properties of detectors, highlighting the importance of carefully managing these transitions during the crystal growth process.

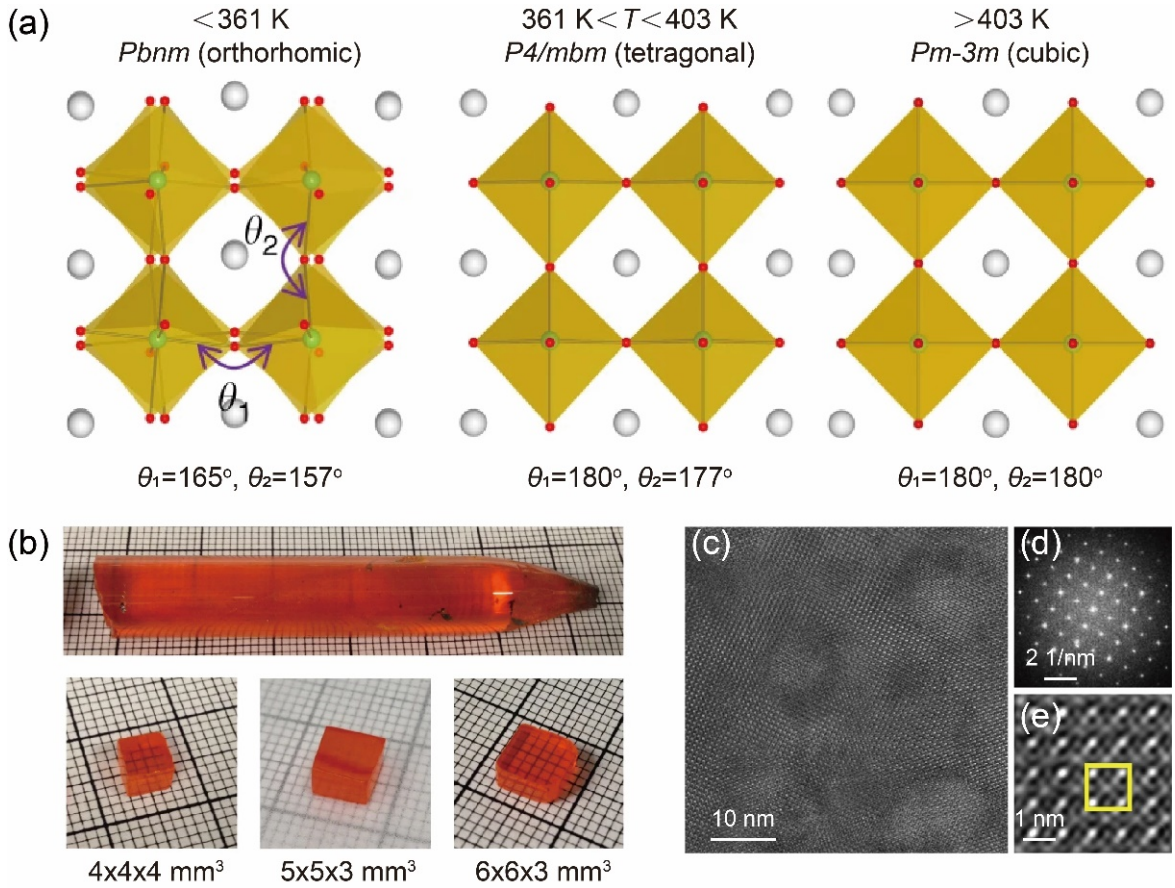


Figure 2. (**a**) Phase transitions in $CsPbBr_3$, during which the $PbBr_6$ octahedra exhibit distortion. (**b**) Photos of as-prepared large-sized $CsPbBr_3$ single crystal. Bottom pictures are the single crystal wafers of different sizes. (**c**) HRTEM picture of 3D $CsPbBr_3$ single crystal. (**d**) The corresponding SAED pattern and (**e**) magnified lattice image. The yellow box is drawn to compare HRTEM image. Reprinted with permission from Ref. [80]. Copyright 2018, Nature Publishing Group.

In a recent study, researchers presented an enhanced Bridgman method for growing $CsPbBr_3$ single crystals, significantly improving their optoelectronic performance [80]. The as-grown $CsPbBr_3$ single crystals, with dimensions reaching several centimeters, exhibit exceptionally low impurity concentrations (below 10 ppm across a total of 69 elements). The critical process in this work is the modification of growth parameters, which leads to large-sized, crack-free single crystals, as shown in Figure 2b. It is important to highlight that the precise control of kinetic parameters during the crystal growth process is critical. Parameters including temperature gradient and cooling rate play pivotal roles, and have been meticulously optimized through growing many times. Notably, the impurity concentration in final products is below 10 ppm, with impurities exceeding 0.5 ppm likely being introduced from the precursor materials. Additionally, the optical transmittance is higher than 65% for wavelengths greater than 600 nm and exceeds 80% for wavelengths above 1000 nm. These findings confirm that the $CsPbBr_3$ single crystals exhibit exceptional chemical purity, which is one of the distinct advantages of the Bridgman method [81]. The single-crystallinity and outstanding uniformity of the $CsPbBr_3$ crystals were verified through selected area electron diffraction (SAED) and high-resolution transmission electron microscopy (HRTEM) with fast Fourier transform (FFT) analysis, as shown in Figure 2c–e. No precipitates were detected in these single crystals, further confirming their high chemi-

cal purity. Consequently, the scalable growth of 3D $CsPbBr_3$ single crystals underscores the potential of metal halides as exceptional next-generation materials for photoelectric applications [82,83].

In another study, large-sized 3D $CsPbBr_3$ single crystals were grown using an optimized Bridgman method, as shown in Figure 3a [23]. After determining the crystallographic directions using the X-ray orientation technique, the anisotropic optoelectronic properties of the material were investigated for the first time. To examine the optoelectronic anisotropy, photoresponse measurements were performed on the (100), (010), and (001) crystallographic planes, as shown in Figure 3b. The three $CsPbBr_3$ single crystal devices possessed distinct anisotropic optoelectronic properties. The responsivity and external quantum efficiency (EQE) of the best plane demonstrated a three-fold improvement compared to other planes. This unique behavior can be attributed to the structural anisotropy of $CsPbBr_3$, which determines the charge carrier's transport. The anisotropic electron-transport properties in $CsPbBr_3$ single crystals were further characterized, as shown in Figure 3c [84]. In the current–voltage curves, Ohmic, trap-filling, and Child regions were detected as the bias voltage increased. These results reveal a pronounced anisotropy in the electron transport properties, with superior electron transport observed along a certain direction. This is due to the variations in the carrier transport within the crystal structure [85–87]. Consequently, the exceptional optoelectronic properties of $CsPbBr_3$ single crystals prepared via the Bridgman method are expected to inspire further exploration of their potential for high-performance optoelectronic applications.

The detection of γ-rays with high energy resolution remains the most challenging applications today [88–90]. Even the smallest presence of defects can significantly degrade the signal generated by γ-rays, making semiconductor detectors relatively rare. However, lead halide perovskite semiconductors exhibit exceptional defect tolerance, resulting in outstanding and unique optoelectronic properties [91–93]. As a result, these materials are poised to have a transformative impact on applications in photoelectric conversion and radiation detection. In a recent study, researchers demonstrated that $CsPbCl_3$ single crystals grown by the Bridgman method can act as high-performance detectors for γ-ray radiation [94]. Similarly to $CsPbBr_3$, $CsPbCl_3$ undergoes two phase transitions: from the cubic to the tetragonal phase at 325 K, followed by a transition to the orthorhombic phase at 316 K, which finally becomes stable at room temperature (Figure 4a) [95]. Large-scale $CsPbCl_3$ single crystals were synthesized using the Bridgman method, as shown in Figure 4b. The resulting $CsPbCl_3$ crystal exhibits pale-yellow with high optical transparency. The optical transmission exceeds 80% for wide light wavelengths, as shown in Figure 4c. This high transparency indicates that $CsPbCl_3$ single crystals contain few impurities. The optical absorption edge was around 425 nm, corresponding to a wide bandgap of 2.90 eV. Therefore, the wide-bandgap $CsPbCl_3$ single crystals obtained through the Bridgman method hold significant potential for γ-ray detection [96–98].

The Bridgman method can also be used to grow 3D metal halide single crystals with mixed compositions [99–102]. In a recent study, series of large-sized perovskite single crystals $CsPbBr_{3-3n}X_{3n}$ were fabricated by the modified Bridgman method through precisely controlling the synthesis parameters, as exhibited in Figure 5a [8]. The sharp absorption edges in the absorption spectra indicate the direct-band-gap feature of these perovskite single crystals, as depicted in Figure 5b. Furthermore, the absorption edges of them are continuously tunable, corresponding to wide bandgaps, by only adjusting the halide composition [103]. Consequently, perovskite single crystals with mixed halogens exhibit considerable potential as filter-free photodetectors.

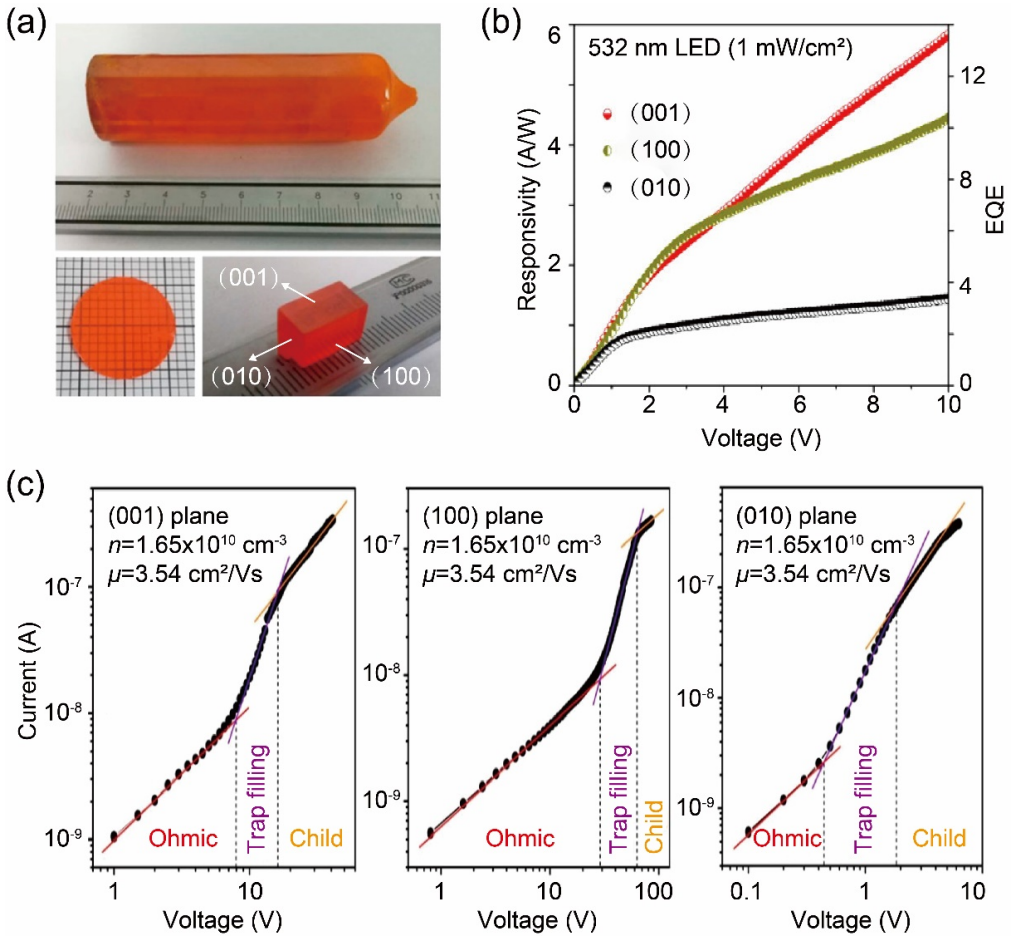


Figure 3. (**a**) Pictures of large-sized $CsPbBr_3$ single crystals (top), cut wafer (bottom left), and cuboid $CsPbBr_3$ single crystals (bottom right). (**b**) Responsivity and EQE for the three crystallographic planes. (**c**) Dark current–voltage features of $CsPbBr_3$ single crystals. Reprinted with permission from Ref. [23]. Copyright 2018, American Chemical Society.

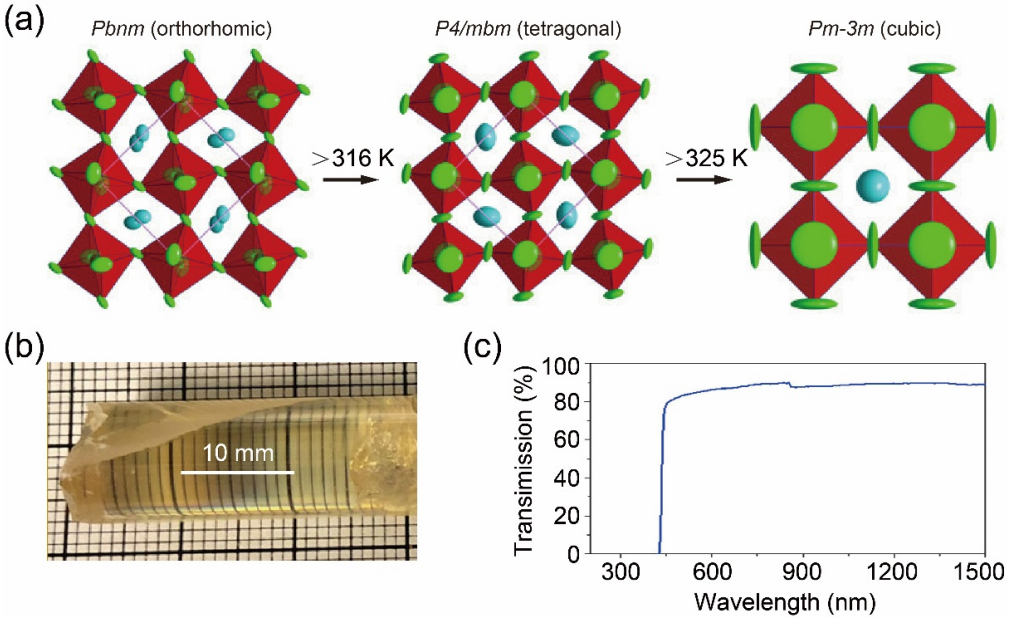


Figure 4. (**a**) Structural evolution of $CsPbCl_3$ near ambient temperature. (**b**) Photograph of $CsPbCl_3$ single crystal grown by the Bridgman method and (**c**) its optical transmission. Reprinted with permission from Ref. [94]. Copyright 2021, American Chemical Society.

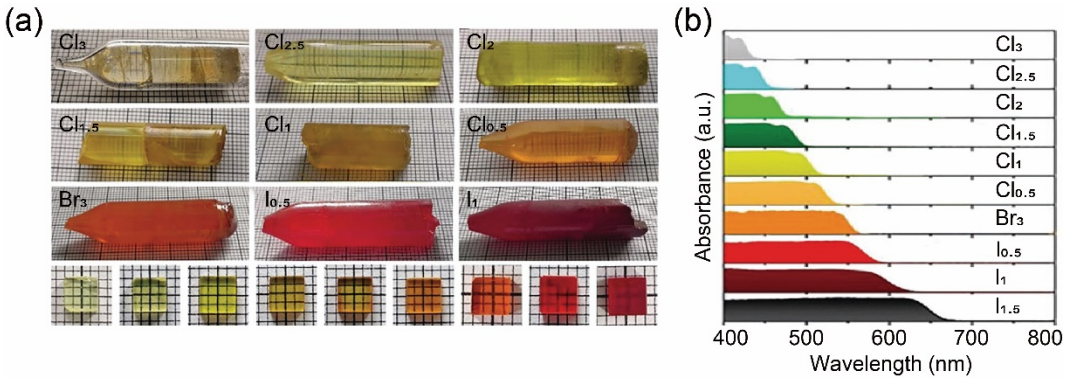


Figure 5. (**a**) Photographs of $CsPbBr_{3-3n}X_{3n}$ single crystals with mixed halogens and (**b**) their corresponding UV–Vis absorption spectra. Reprinted with permission from Ref. [8]. Copyright 2021, Royal Society of Chemistry.

3. Bridgman Method for Growing Two-Dimensional Metal Halide Single Crystals

The two-dimensional (2D) Ruddlesden–Popper (RP) phases constitute a significant class of metal halides, characterized by their diverse and remarkable optoelectronic properties [104–106]. To date, the majority of hybrid RP phases incorporate long organic spacers [107,108]. However, conventional synthesis methods are predominantly limited to the growth of 2D RP metal halides with organic components. In another word, all-inorganic 2D RP metal halides cannot be prepared. In other words, synthesizing all-inorganic 2D RP metal halides presents significant challenges.

Recent studies have successfully synthesized all-inorganic 2D RP $Cs_2PbI_2Cl_2$ single crystals using the Bridgman method, as shown in Figure 6a [79,109]. These crystals are nearly centimeter-sized, significantly larger than those obtained through solution-based methods. $Cs_2PbI_2Cl_2$ adopts the K_2NiF_4-type configuration and crystallizes in tetragonal phase, as illustrated in Figure 6b–d [110]. The 2D $[PbI_2Cl_2]^{2-}$ plane is composed of corner-sharing Pb-centered $[PbI_2Cl_4]^{4-}$ units. In addition, Cl^- ions occupy in-plane sites, behaving as shared corners of octahedra, while I^- ions occupy out-of-plane sites as terminal ligands. Cs^+ spacer ions balance the charge, resulting in a standard single-layer (n = 1) RP structure. Density functional theory calculations, along with experimental findings, support the thermodynamic stability of these single crystals. Further computational analysis indicates that $Cs_2PbI_2Cl_2$ behaves as a direct bandgap semiconductor with low effective carrier mass towards in-plane direction, which aligns with the experimentally obtained in-plane photoresponse [111,112]. The successful growth of $Cs_2PbI_2Cl_2$ by the Bridgman method not only expands the family of 2D metal halides but also opens new possibilities for applications beyond photovoltaics.

Subsequent efforts were made by researchers to grow larger single crystals using the Bridgman method. Through meticulous adjustment of synthesis parameters, including the cooling rate, temperature gradient, and post-heat treatment, large-sized single crystals were successfully achieved, as exhibited in Figure 7a [113]. Structural analysis reveals that the single-layer RP structure is composed of corner-sharing $[PbI_2Cl_4]^{4-}$ octahedral units, as depicted in Figure 7b. Further investigations confirm that the remarkable phonon transport properties of $Cs_2PbI_2Cl_2$, driven by lone-pair-driven octahedral rotations and anharmonic lattice dynamics, which demonstrates the potential for novel thermal transport behavior across a broad range of low-dimensional metal halide perovskites [114].

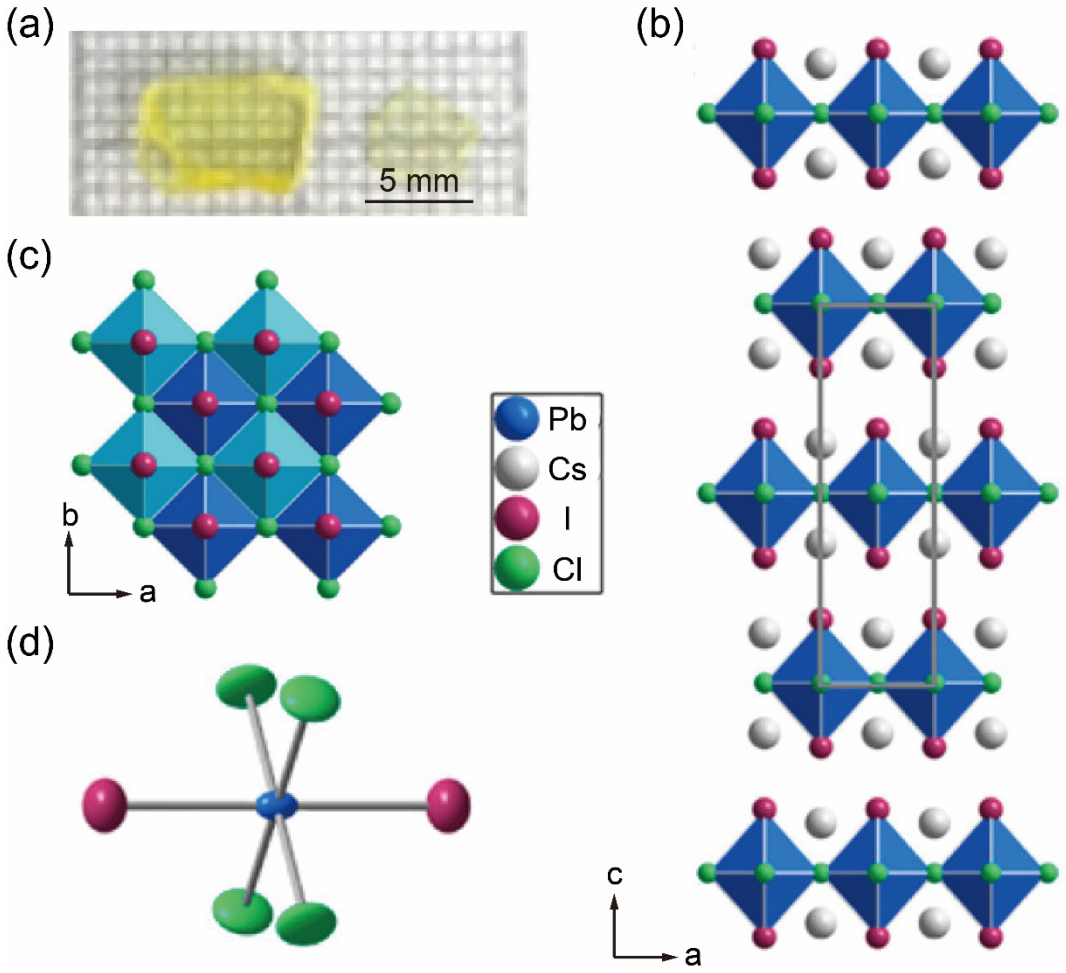


Figure 6. (**a**) Picture of $Cs_2PbI_2Cl_2$ single crystal grown using the Bridgman method. Crystal structure of $Cs_2PbI_2Cl_2$, shown from (**b**) the side view and (**c**) the top-down view. Additionally, (**d**) depicts the elongated $[PbI_2Cl_4]^{4-}$ octahedral unit. Reprinted with permission from Ref. [109]. Copyright 2018, American Chemical Society.

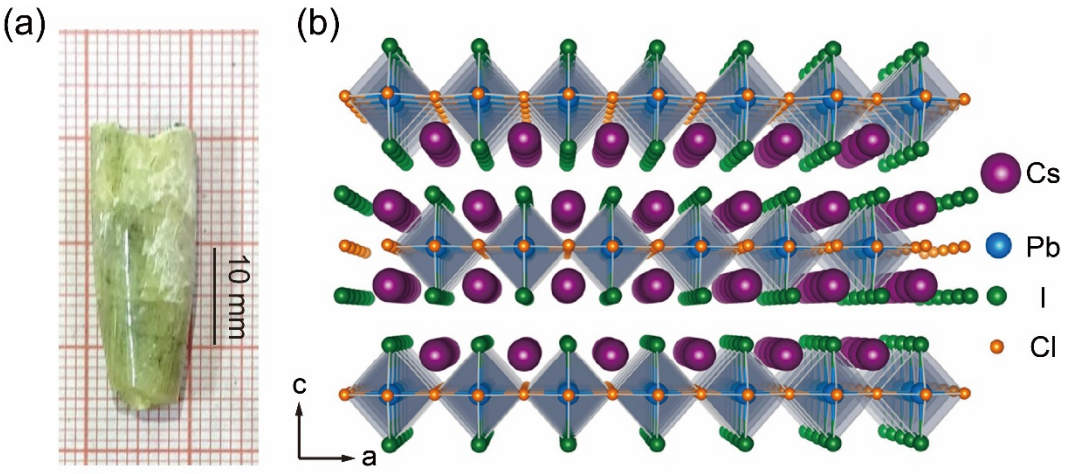


Figure 7. (**a**) Picture of $Cs_2PbI_2Cl_2$ single crystals prepared by the Bridgman method. (**b**) Crystal structure of the 2D RP metal halide $Cs_2PbI_2Cl_2$. Reprinted with permission from Ref. [113]. Copyright 2020, American Chemical Society.

4. Bridgman Method for Growing Zero-Dimensional Metal Halide Single Crystals

In recent years, less toxic metals such as Sn, Sb, and Bi have attracted considerable attention as environmentally friendly alternatives to Pb [115–119]. Among these, low-dimensional Bi-based halide materials have emerged as promising candidates for optoelectronic applications [120–122]. Notably, all-inorganic zero-dimensional (0D) bismuth-halide single crystals of $Cs_3Bi_2X_9$ (X = Br and I) have been successfully synthesized using the Bridgman method.

As shown in Figure 8a, a custom-designed semitransparent Bridgman furnace has been developed to enable real-time monitoring and precise adjustment of crystal growth parameters during the synthesis process [123]. This innovative furnace facilitated the optimization of the thermal profile for growing high-quality $Cs_3Bi_2Br_9$ single crystals, as illustrated in Figure 8b. Using this modified Bridgman method, large-sized single crystals $Cs_3Bi_2Br_9$ were successfully synthesized. To minimize structural defects and prevent crystal cracking, small temperature gradient and slow growth rates have been proved essentially. Specifically, slower rates were employed to grow transparent, crack-free $Cs_3Bi_2Br_9$-2 crystals, while faster rates resulted in cracked $Cs_3Bi_2Br_9$-1 crystals, as shown in Figure 8c. Figure 8d displays the optical transmittance spectra of these two single crystals. Both exhibit a broad transparency range with no significant absorption features. Notably, $Cs_3Bi_2Br_9$-2 demonstrates an average transmittance of approximately 80% in the range of 2 μm to over 18 μm, surpassing the ~70% transmittance of $Cs_3Bi_2Br_9$-1. At room temperature, $Cs_3Bi_2Br_9$ crystallizes into trigonal system, with its crystal structure depicted in Figure 8e [124]. The layered perovskite structure of $Cs_3Bi_2Br_9$ can be regarded as a tripling of typical perovskite unit cell, where only partial octahedra are fully occupied. The remaining octahedra form corrugated, vacant layers that separate the occupied layers. This arrangement enables a corner-sharing configuration of $[BiBr_6]^-$ octahedra [125].

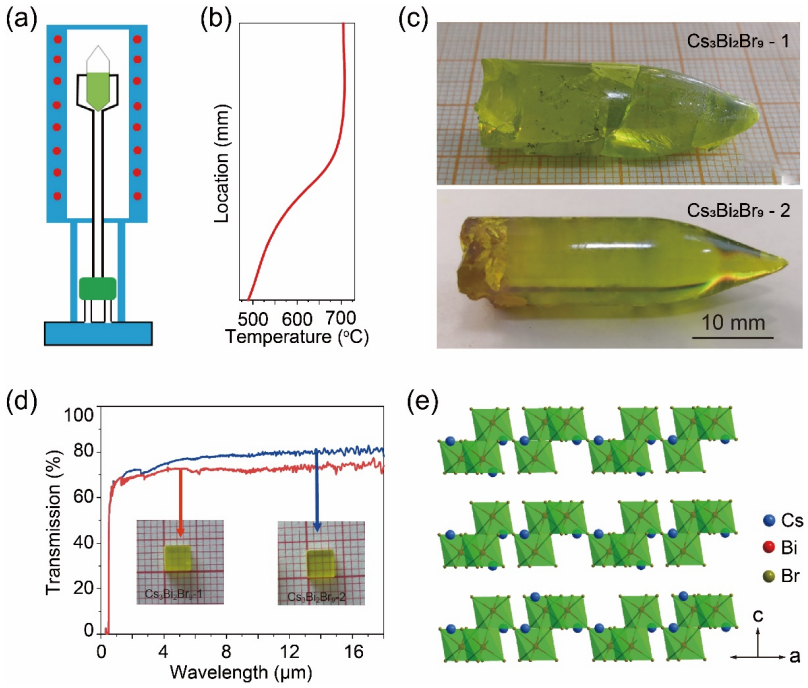


Figure 8. (**a**) Schematic illustration of the Bridgman method used for the synthesis of $Cs_3Bi_2Br_9$ single crystals. (**b**) The optimized thermal profile. (**c**) Pictures of $Cs_3Bi_2Br_9$-1 (top) and $Cs_3Bi_2Br_9$-2 (bottom). (**d**) Transmission spectra of $Cs_3Bi_2Br_9$-1 and $Cs_3Bi_2Br_9$-2. Insets show the oriented (−1 2 0) planes of these two single crystals. (**e**) Crystal structure of $Cs_3Bi_2Br_9$. Reprinted with permission from Ref. [123]. Copyright 2021, Science China Press.

Subsequently, researchers proposed a mixed-halogen strategy to fine-tune the structural dimensions and optoelectronic properties of $Cs_3Bi_2I_{9-n}Br_n$ [126]. High-quality single crystals, with dimensions reaching up to ten centimeters, were successfully grown using the Bridgman technique, as depicted in Figure 9a. By incorporating iodine into the 0D $Cs_3Bi_2Br_9$ framework, the optoelectronic properties were systematically modified. Among these, $Cs_3Bi_2I_8Br$ emerged as the most promising candidate, demonstrating negligible ion migration, moderate resistivity, and superior carrier transport capabilities. The halogen-mixing strategy offers a pathway to balance carrier transport properties with resistivity in targeted compositions, optimizing performance for applications such as X-ray detection. Notably, $Cs_3Bi_2I_8Br$ was identified as the optimal composition, achieving a record-breaking sensitivity of 1.74×10^4 μC Gy^{-1} cm^{-2}. This sensitivity is second only to the 6.3×10^4 μC Gy^{-1} cm^{-2} achieved by Pb-based $CsPbBr_{2.9}I_{0.1}$ single crystals under 120 keV hard X-ray detection. Furthermore, X-ray detectors fabricated from $Cs_3Bi_2I_8Br$ single crystals demonstrated exceptional long-term stability in ambient air, ultralow dark current drift, and robust high-resolution imaging performance even at elevated temperatures. This combination of properties underscores the material's potential for next-generation X-ray detection technologies [127,128].

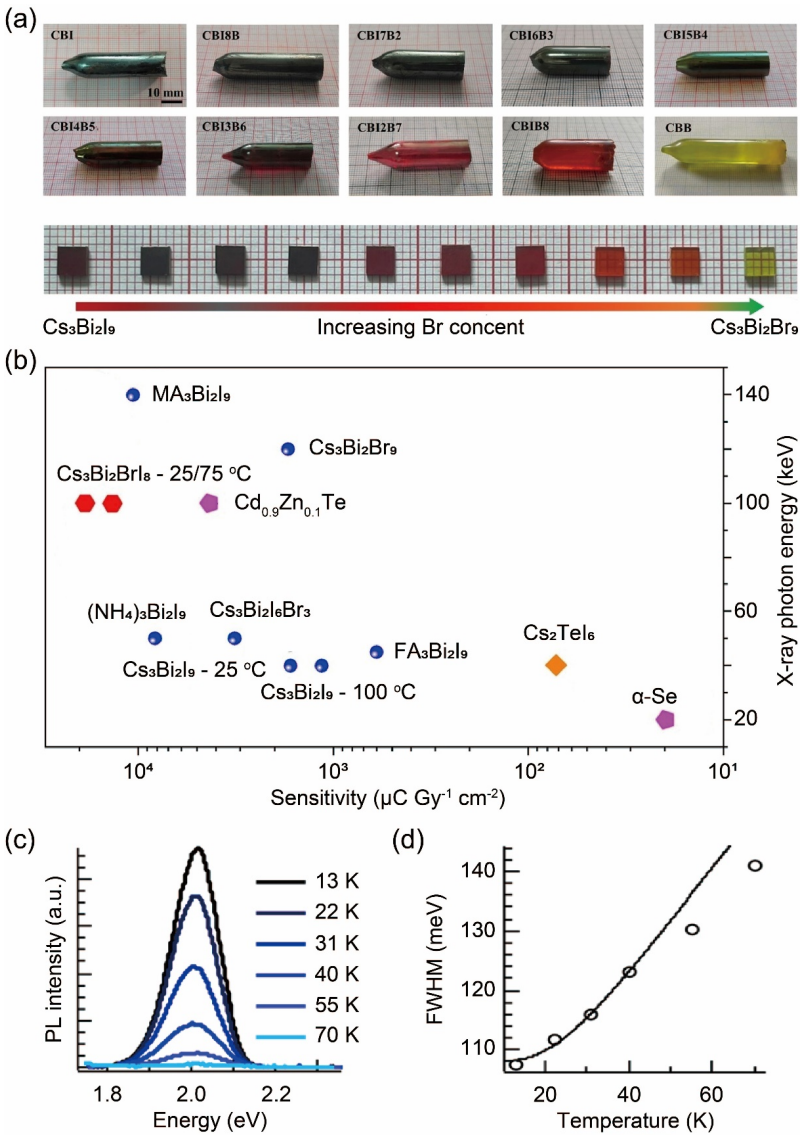


Figure 9. (**a**) Photographs of as-grown $Cs_3Bi_2I_{9-n}Br_n$ single crystals and their corresponding (001)-oriented plates. (**b**) Comparison of sensitivities between Pb-free perovskite single crystals, commercial

CdZnTe single crystals, and commercial α-Se. Reprinted with permission from Ref. [126]. Copyright 2023, Wiley-VCH GmBH. (**c**) Temperature-dependent photoluminescence spectra of $Cs_3Sb_2I_9$ at 5 mW excitation power. (**d**) Temperature-dependent FWHM fitted using *H-S* equation. Reprinted with permission from Ref. [129]. Copyright 2017, American Chemical Society.

The optical and electronic properties of Bridgman-grown single crystals of wide-bandgap semiconducting halide perovskites $A_3M_2I_9$ (A = Cs, Rb; M = Bi, Sb) have been extensively studied [130]. Intense Raman scattering was observed at room temperature for all compounds, indicating high polarizability and pronounced electron–phonon coupling [129]. Strong evidence of electron–phonon interactions, comparable to those found in alkali halides, was revealed through phonon broadening in the photoluminescence emission spectra, as shown in Figure 9c,d. Effective phonon energies, derived from temperature-dependent photoluminescence measurements, aligned well with the observed Raman peak energies. Based on these findings, a model has been proposed wherein electron–phonon interactions in $Cs_3Sb_2I_9$, $Rb_3Sb_2I_9$, and $Cs_3Bi_2I_9$ generate small polarons, resulting in exciton trapping by the lattice. The recombination of these self-trapped excitons accounts for the broad photoluminescence emission. Additionally, $Rb_3Bi_2I_9$, $Rb_3Sb_2I_9$, and $Cs_3Bi_2I_9$ exhibit high resistivity and strong photoconductive responses under laser photoexcitation. These characteristics suggest that these compounds are promising candidates for semiconductor applications, particularly in the detection of hard radiation.

5. Bridgman Method for Growing Novel Metal Halide Single Crystals

5.1. $Cs_3Cu_2I_5$ Single Crystals

Low-dimensional Cu(I) metal halides, known for their efficient exciton emissions, have recently gained attention as promising scintillation materials for X-ray and gamma-ray detection [131–133]. A recent study demonstrated the potential of 0D $Cs_3Cu_2I_5$ as a sensitive thermal neutron detector with effective neutron–gamma discrimination achieved through lithium doping [134,135]. Single crystals of $Cs_3Cu_2I_5$ doped with 95% enriched ^{6}Li were successfully grown using the Bridgman method, as illustrated in Figure 10a. As shown in Figure 10b, $Cs_3Cu_2I_5$:^{6}Li exhibits impressive performance metrics, including an energy resolution of 4.8% for 662 keV ^{137}Cs gamma rays, a high light yield of 30,000 photons/MeV for gamma rays, and 96,000 photons/neutron for thermal neutrons. Additionally, it achieves a robust neutron–gamma pulse shape discrimination figure of merit of 2.27 using Power Spectral Density (PSD) waveforms. This breakthrough discovery of 0D metal halide single crystals, specifically $Cs_3Cu_2I_5$:^{6}Li, represents a significant advancement in the development of stable, high-performance scintillators for neutron–gamma detection applications [136,137].

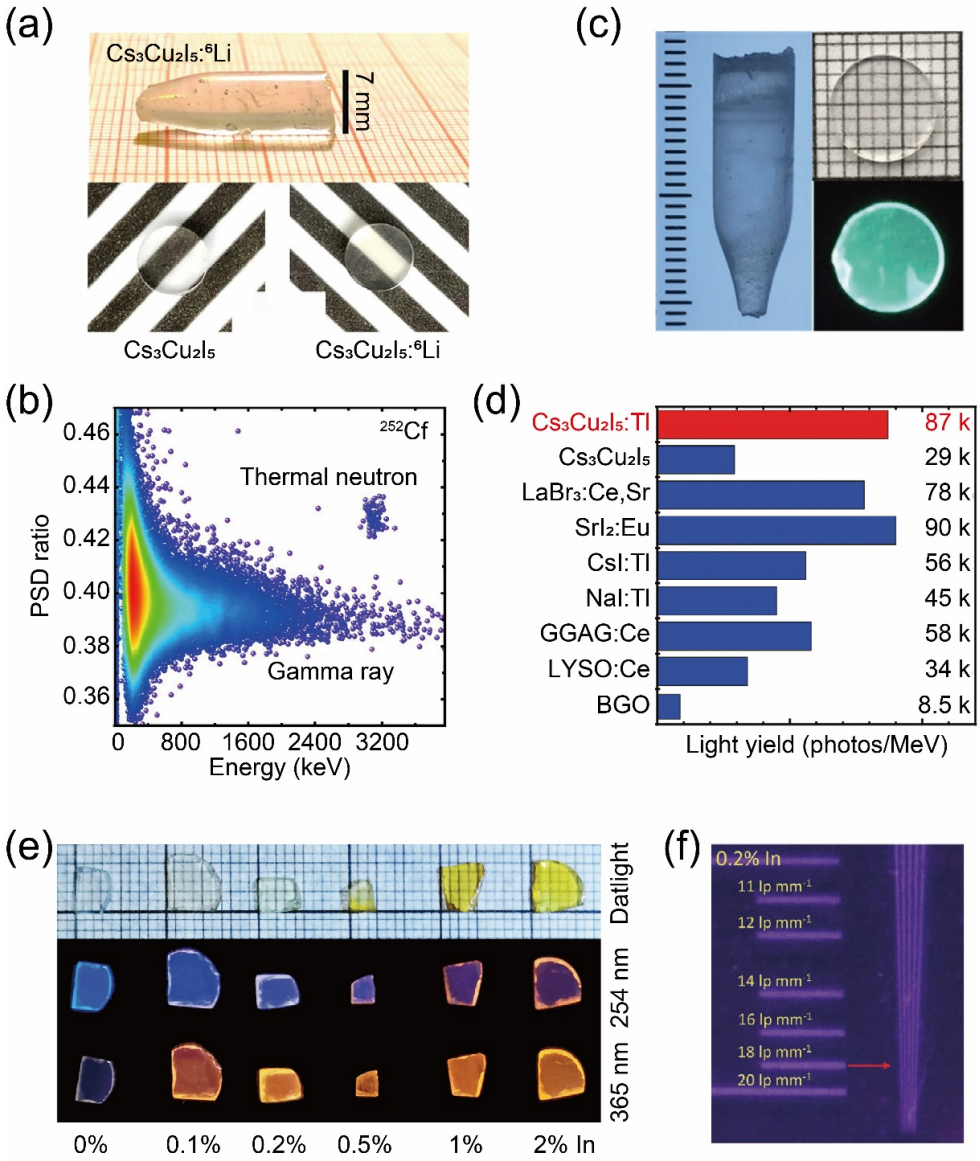


Figure 10. (**a**) As-grown $Cs_3Cu_2I_5$:^{6}Li crystal ingot with a 7 mm diameter (top) and polished $Cs_3Cu_2I_5$ (bottom left) and $Cs_3Cu_2I_5$:^{6}Li (bottom right) slabs. (**b**) PSD scatter plot and one-dimensional histogram of a $Cs_3Cu_2I_5$:^{6}Li single crystal upon excitation with a ^{252}Cf source and a ^{137}Cs source. Reprinted with permission from Ref. [134]. Copyright 2022, American Chemical Society. (**c**) As-grown 7 mm diameter Tl-doped $Cs_3Cu_2I_5$ crystal ingot, and a 1 mm thick sample under daylight and ultraviolet light. (**d**) Comparison of absolute light yield between Tl-doped $Cs_3Cu_2I_5$:Tl, undoped $Cs_3Cu_2I_5$, and other conventional scintillators. Reprinted with permission from Ref. [138]. Copyright 2021, Wiley-VCH GmBH. (**e**) $Cs_3Cu_2I_5$:In crystal slabs under daylight, 254 nm, and 365 nm UV light illumination. (**f**) X-ray 2D spatial images of the test-pattern plate using 0.2% In-doped $Cs_3Cu_2I_5$ single crystals. Reprinted with permission from Ref. [139]. Copyright 2022, Wiley-VCH GmBH.

In another study, Tl cations were successfully incorporated into the $Cs_3Cu_2I_5$ host using the Bridgman method, leading to the development of an ultrabright and highly efficient scintillator for X-ray and γ-ray detection, as shown in Figure 10c [138]. The Tl-doped $Cs_3Cu_2I_5$ single crystals achieved an impressive photoluminescence quantum efficiency of 79.2%. Under X-ray excitation, the radioluminescence emission of $Cs_3Cu_2I_5$:Tl crystals featured a self-trapped exciton emission at 440 nm and a Tl-related emission at 510 nm at room temperature. Optimized Tl doping resulted in a nearly fivefold enhancement of the steady-state scintillation yield, reaching up to 150,000 photons/MeV, alongside a significant improvement in X-ray detection sensitivity, which decreased from 103.6 to

66.3 nGy s^{-1}. Additionally, the material exhibited an exceptionally low afterglow of just 0.17% at 10 ms after X-ray cutoff. The $Cs_3Cu_2I_5$:Tl scintillator demonstrated outstanding performance, including an energy resolution of 3.4% at 662 keV and an ultrahigh light yield of 87,000 photons/MeV under ^{137}Cs γ-ray radiation, rivaling the capabilities of commercial scintillators, as illustrated in Figure 10d [140,141].

Based on the aforementioned studies, it can be concluded that doping-modified $Cs_3Cu_2I_5$ single crystals exhibit significant potential as X-ray detection materials, primarily due to their efficient exciton emissions arising from strongly localized charge carriers [142–147]. However, many of these materials still display scintillation yields well below their theoretical maxima [148]. A recent study demonstrated that the charge carrier harvesting efficiency could be significantly enhanced by introducing a small amount of indium (In) doping into these highly localized structures [139]. Bright 0D $Cs_3Cu_2I_5$:In single crystals were synthesized via the Bridgman method, exhibiting efficient and tunable dual emissions. All samples were transparent and free of inclusions, as shown in Figure 10e. Under X-ray excitation, the radioluminescence emission of $Cs_3Cu_2I_5$:In crystals featured a self-trapped exciton emission at 460 nm and an In^+-related emission at 620 nm at room temperature. In doping significantly enhanced the photoluminescence quantum efficiency of $Cs_3Cu_2I_5$from 68.1% to 88.4%. To assess the impact of In doping on X-ray imaging performance, undoped and 0.2% In-doped $Cs_3Cu_2I_5$ single crystals were utilized as scintillation screens in an X-ray imaging system. As depicted in Figure 10f, the In-doped $Cs_3Cu_2I_5$ crystals achieved an exceptional spatial resolution of 18 lp mm^{-1}, surpassing commercial CsI:Tl-based flat-panel X-ray detectors, all-inorganic perovskite nanocrystal scintillators, and thermally activated delayed fluorescence (TADF) organic scintillator-based X-ray imaging detectors (≈6 lp mm^{-1}) [52,149]. This remarkable spatial resolution is attributed to the superior transparency, reduced light scattering, and enhanced scintillation yield of $Cs_3Cu_2I_5$ single crystals compared to commercial polycrystalline thick films or fluorescent powders. These advancements position $Cs_3Cu_2I_5$:In as a highly promising candidate for next-generation X-ray imaging applications.

5.2. Tl-Containing Single Crystals

Materials containing thallium (Tl) often exhibit strong fluorescence, making Tl-doped crystals highly suitable as scintillators for high-energy radiation detection [150–153]. In fact, such scintillators are widely utilized today. For instance, Tl-doped sodium antimonite (NaSb:Tl) crystals are known for their high scintillation efficiency and excellent radiation response, making them a common choice for particle detectors [150]. Additionally, Tl-doped magnesium aluminate ($MgAl_2O_4$:Tl) is recognized for its exceptional thermal stability and high light output, while Tl-doped cesium chloride (CsCl:Tl) is frequently employed for neutron detection, as Tl significantly enhances the material's sensitivity to neutrons [154–157]. Similarly, Tl-doped cesium fluoride (CsF:Tl) scintillators exhibit a high light yield, making them ideal for radiation detection and particle physics experiments. As a result, Tl-containing scintillators are extensively applied across diverse fields, including nuclear physics, radiation monitoring, medical imaging, and particle detection, underscoring their importance in advancing high-energy detection technologies [158].

In a recent study, centimeter-sized $TlPbI_3$ single crystals were successfully grown using the Bridgman method, as illustrated in Figure 11a [159]. $TlPbI_3$ exhibits a unique crystal structure within the halides, distinguishing itself from conventional perovskites by belonging to the broader class of perovskite-like compounds. It crystallizes in the orthorhombic space group Cmcm and adopts the $CaIrO_3$ structure type, as shown in Figure 11b [160]. The structure consists of alternating layers of $[PbI_3]^-$ units interspersed with Tl^+ ions. Within the 2D layers, the axially compressed $[PbI_{6/2}]^-$ octahedra expand

anisotropically in the perovskite plane. These octahedra are connected via edge-sharing ($PbI_4/_2$ connectivity) along the shorter a-axis and corner-sharing ($PbI_2/_2$ connectivity) along the longer c-axis. The Tl atoms adopt a trigonal prismatic coordination geometry [161]. The bandgap structure of $TlPbI_3$ is mainly determined by Pb 6s and Tl 6s states deriving from the lone pair electrons in Pb^{2+} and Tl^+ [159]. As we all know, metal elements often result in quite different electronic structures and properties in halide compounds [162,163]. The 5s electron pair of Pb^{2+} results in high tolerance against defects, therefore better stability of $TlPbI_3$ is often obtained than their counterparts such as $CsPbI_3$ [164]. Another study indicates that stronger bonding between Tl and I is the main cause of better stability of $TlPbI_3$ than $CsPbI_3$, owing to the lower total energy [165]. Furthermore, due to their different configurations of perovskite structure in $CsPbI_3$ and perovskite-like structure in $TlPbI_3$, they possess significantly disparate properties. For example, stronger bonding interactions in TlPbI3 lead to more dispersive band edges, which increases the bandwidth and reduces the bandgap [166]. Moreover, the enhanced dispersion of band edges makes less effective carrier masses and anisotropic transport features.

$TlPbI_3$ demonstrates high electrical resistivity of approximately 10^{12} Ω·cm. Detectors fabricated from these single crystals show robust photoresponsiveness to Ag Kα X-rays (22.4 keV) and are capable of detecting 122 keV γ-rays from a ^{57}Co radiation source. The electron mobility-lifetime product was measured at 1.8×10^{-5} $cm^2 \cdot V^{-1}$. Furthermore, $TlPbI_3$ exhibits a high relative static dielectric constant of 35.0, indicating its strong capability to screen carrier scattering and suppress the effects of charged defects. These characteristics position $TlPbI_3$ as a promising material for high-energy radiation detection applications [164,166,167].

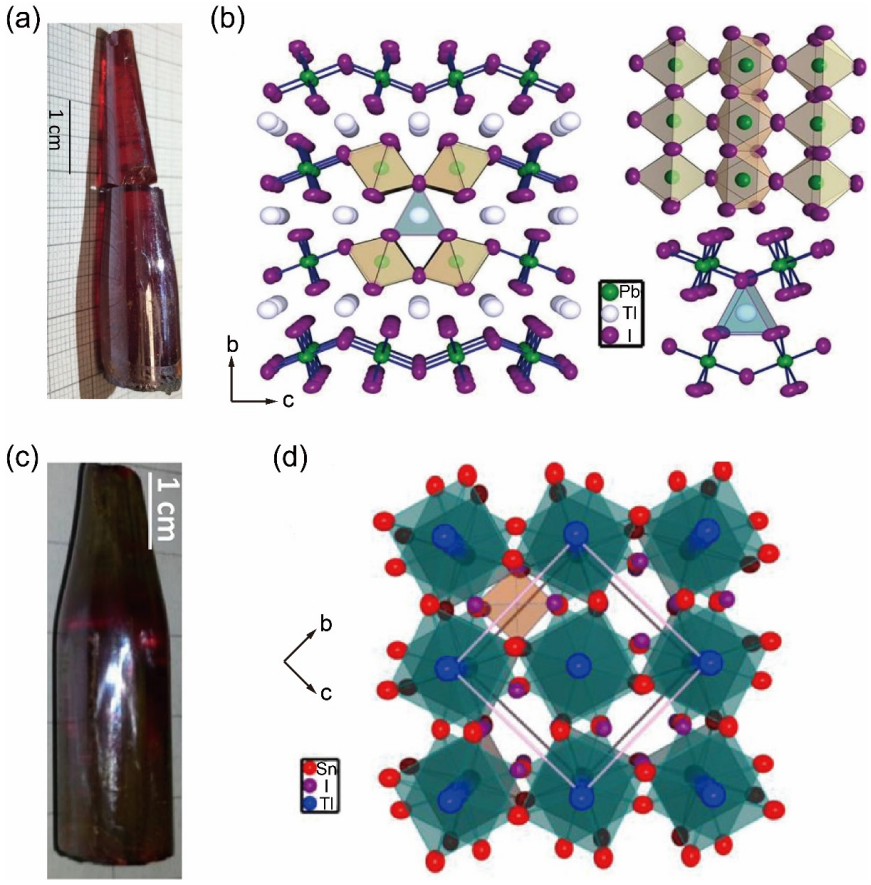


Figure 11. (**a**) Image of a pristine $TlPbI_3$ single crystal. (**b**) The crystal structure of $TlPbI_3$ with the left panel providing an overview of the structure. The right panels focus on the connectivity along the

$[PbI_3]^-$ layers and the coordination environment around the Tl^+ ions, respectively. Reprinted with permission from Ref. [159]. Copyright 2021, Wiley-VCH GmBH. (**c**) Image of the $TlSn_2I_5$ single crystal. (**d**) The antiperovskite structure of $TlSn_2I_5$. Reprinted with permission from Ref. [168]. Copyright 2017, American Chemical Society.

In addition to $TlPbI_3$, the semiconductor $TlSn_2I_5$, which features a two-dimensional crystal structure and an antiperovskite topology, has emerged as a promising novel material for radiation detection applications [169]. $TlSn_2I_5$ incorporates elements with high atomic numbers (Tl: 81, Sn: 50, I: 53) and a relatively high density (6.05 $g \cdot cm^{-3}$), ensuring a superior absorption coefficient compared to both halide perovskites and CdZnTe in response to hard radiation. In a recent study, centimeter-sized $TlSn_2I_5$ single crystals were successfully grown using the Bridgman method, as shown in Figure 11c [168]. As illustrated in Figure 11d, when viewed without considering chemical bonding constraints, the lattice formed by I, Tl, and Sn adopts an antiperovskite structure. In this arrangement, iodine is positioned at the center of an axially elongated octahedron, with its equatorial plane occupied by four Sn ions and its polar positions filled by two Tl ions. This results in the formation of a cationic $[ISn_2Tl]^{4+}$ framework. This framework exhibits a distorted perovskite structure, with the octahedra tilting out-of-phase in a manner similar to that observed in the hybrid perovskite $CH_3NH_3PbI_3$, which crystallizes in the non-centrosymmetric I4/mcm space group due to the asymmetric CH_3NH_3 $^+$cation. However, compared to $CH_3NH_3PbI_3$, $TlSn_2I_5$ demonstrates superior long-term stability, enhanced photon stopping power, higher resistivity (~10^{10} $\Omega \cdot cm$), and robust mechanical properties. Additionally, $TlSn_2I_5$ can be utilized to fabricate detector devices capable of detecting Ag Kα X-rays (22 keV), ^{57}Co γ-rays (122 keV), and ^{241}Am α-particles (5.5 MeV). The mobility-lifetime product and electron mobility were estimated to be 1.1 $\times$ 10^{-3} $cm^2 \cdot V^{-1}$ and 94 $\pm$ 16 $cm^2 \cdot V^{-1} \cdot s^{-1}$, respectively. Notably, unlike other halide perovskites, $TlSn_2I_5$ exhibits no evidence of ionic polarization under prolonged high-voltage bias, further highlighting its suitability for long-term, stable operation in radiation detection applications.

5.3. Zero-Dimensional A_2BX_6 Perovskite Single Crystals

Zero-dimensional halide perovskites with the A_2BX_6 (A = Cs, Rb; B = Hf, Zr, Te, Ti; X = Cl, Br, I) structure represent a distinct class of materials, exhibiting unique physicochemical properties [170–178]. These A_2BX_6 halide perovskites are notable for their lack of extension into higher-dimensional crystal networks. Instead, they exist as isolated molecules or clusters. This structural characteristic leads to highly localized electronic states, which in turn result in exceptional optoelectronic properties, including efficient light absorption and emission. Additionally, in contrast to higher-dimensional metal halide perovskites, A_2BX_6 perovskites demonstrate superior chemical stability under certain conditions, owing to their more localized structure.

In a recent study, large-scale Cs_2ZrCl_6:Ce,Li single crystals with exceptional energy resolution were successfully synthesized by optimizing the temperature gradient and growth rate using the Bridgman method, as shown in Figure 12a [179]. Single-crystal diffraction analyses confirm the formation of 0D perovskite structures. Specifically, Zr^{4+} cations are coordinated with Cl^- ions to form discrete octahedra, which are isolated by Cs^+ ions, as depicted in Figure 12b [53]. Further investigations reveal that this effective dual-ion co-substitution strategy makes the Cs_2ZrCl_6 single crystal an environmentally friendly material, with promising applications in solar-blind ultraviolet optoelectronics and X-ray detection [180–182].

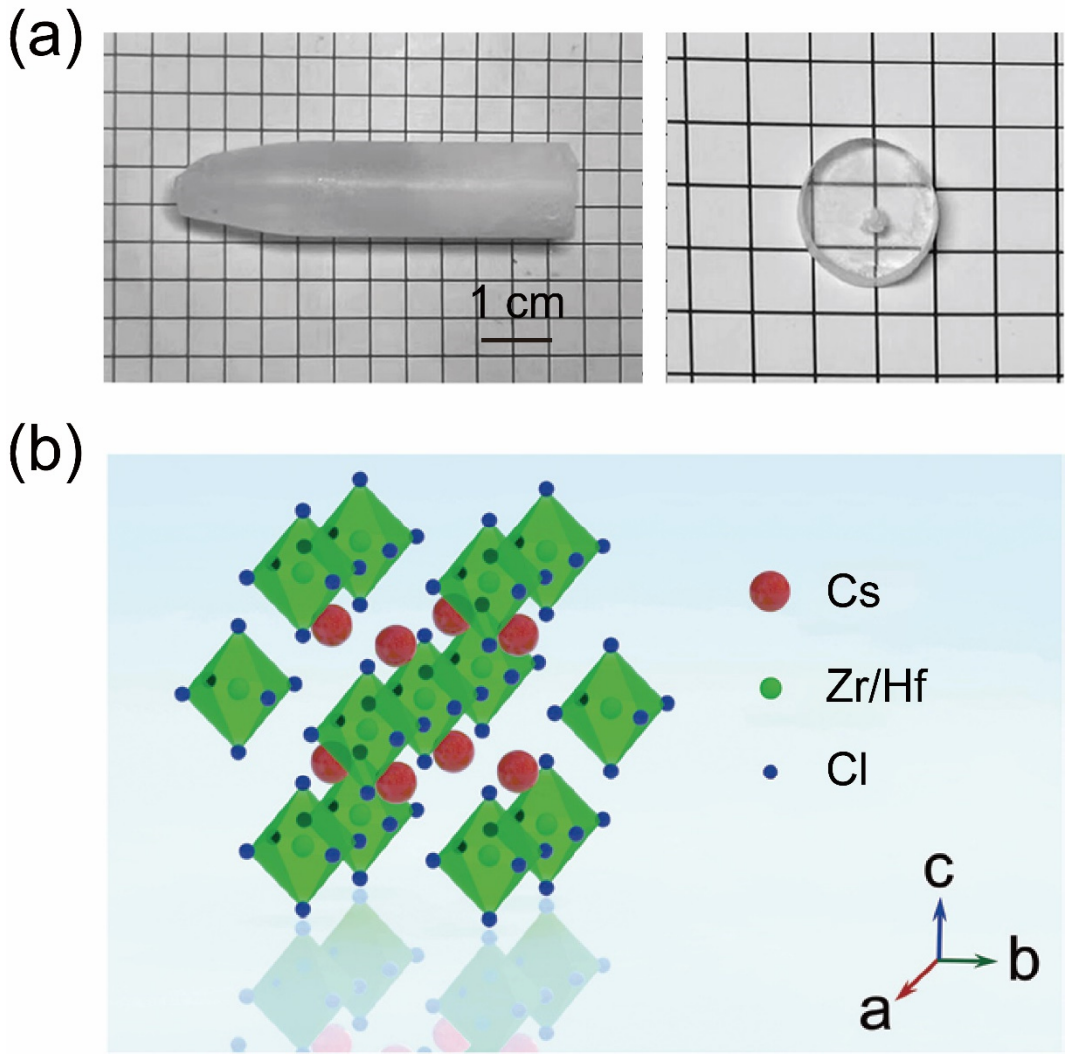


Figure 12. (**a**) As-grown Cs_2ZrCl_6:Ce,Li single crystal (left) and its wafer (right). Reprinted with permission from Ref. [179]. Copyright 2023, American Chemical Society. (**b**) Atomic structure of 0D perovskite crystal. Reprinted with permission from Ref. [53]. Copyright 2022, Wiley-VCH GmbH.

6. Conclusions and Perspectives

As a traditional single-crystal growth technique, the Bridgman method has been extensively employed in the preparation of single crystals for a wide range of materials. In the field of metal halide crystal research, the Bridgman method has played a crucial role, significantly advancing both the fundamental understanding and practical applications of halide materials. Based on the metal halide compositions discussed in this review, we summarize the growth parameters of different metal halide single crystals using the Bridgman method, as shown in Table 1.

Table 1. Growth parameters of metal halide single crystals using the Bridgman method.

Materials	Substance	Temperature Gradient (°C/cm)	Growth Rate	References
$CsPbX_3$	CsX, PbX_2	10–30	0.2–1 mm/hour	[8]
$CsPbBr_3$	CsBr, $PbBr_2$	30–40	1 mm/hour	[23]
$CsPbBr_3$	CsBr, $PbBr_2$	50–70	0.2–0.6 mm/hour	[76,183]
$CsPbBr_3$	CsBr, $PbBr_2$	5–20	0.5–2 mm/hour	[80]
$CsPbCl_3$	CsCl, $PbCl_2$	5–20	0.1–1 mm/hour	[94]

Table 1. *Cont.*

Materials	Substance	Temperature Gradient (°C/cm)	Growth Rate	References
γ-CuCl	CuCl	20	8 mm/day	[30]
γ-CuBr	CuBr	5	6 mm/day	[35]
$CsPbBr_3$	CsBr, $PbBr_2$	10	3–30 mm/hour	[79]
PbI_2	PbI2	22	0.5–1.0 mm/hour	[41]
$TlSn_2I_5$	Sn, I_2, TlI	23		[168]
Tl_2HfX_6	TlX, HfX_4	/	0.2–1 mm/hour	[150]
Tl_2LaX_5	TlX, LaX_3	/	0.2–1 mm/hour	[150]
$A_3M_2I_9$ (A = Cs, Rb; M = Bi, Sb)	$Cs_3Sb_2I_9$: Sb_2O_3, HI, Cs_2CO_3; $Cs_3Bi_2I_9$: Bi_2O_3, HI, CsI; $Rb_3Bi_2I_9$: BiI_3, RbI	/	2 mm/hour	[129,130]
$TlPbI_3$	TlI, PbI_2	12	20 mm/day	[167]
$TlPbI_3$	Tl, Pb, I_2	8	0.5 mm/hour	[159]
Eu-doped $TlSr_2I_5$	TlI, SrI_2, EuI_2	/	10 mm/day	[152]
Bi-doped $CsCdX_3$	CsX, CdX_2, BiX_3	/	2 mm/hour	[162]
Sn-doped $CsPbX_3$	CsX, PbX_2, SnX_2	/	1.4 mm/hour	[61]
Bi-doped $TlCdCl_3$	TlCl, $CdCl_2$, $BiCl_3$	/	1 mm/hour	[163]
$Cs_2PbI_2Cl_2$	CsI, $PbCl_2$	/	0.7 mm/hour	[109]
$Cs_2PbI_2Cl_2$	CsI, $PbCl_2$	/	0.77 mm/hour	[113]
$Cs_3Bi_2Br_9$	CsBr, $BiBr_3$	10–20	0.5–3.0 mm/hour	[123]
$Cs_3Bi_2I_8Br$	CsI, $BiBr_3$	15	1 mm/hour	[126]
^{6}Li-doped $Cs_3Cu_2I_5$	CsI, CuI, ^{6}LiI	/	0.4 mm/hour	[134]
Tl-doped $Cs_3Cu_2I_5$	CsI, CuI, TlI	20–30	0.5–1.0 mm/hour	[138]
Ce,Li-doped Cs_2ZrCl_6	CsCl, $ZrCl_4$, $CeCl_3$, LiCl	15	0.7 cm/day	[179]

Up to now, metal halide single crystals grown by the Bridgman method have been widely used in various fields. For example, high-quality $CsPbBr_3$, $CsPbCl_3$, and $TlPbI_3$ single crystals demonstrate high resolution X-ray detection feature [80,94,159]. ^{6}Li-doped Cs_3CuI_5 single crystals show great potential as scintillator for neutron discrimination [134]. In addition, Er-doped $CsCdBr_3$ single crystals possess unique up conversion capability that can convert low-energy photon to high-energy light, which shows great potential in solar cells [77].

While the Bridgman method offers numerous advantages, it also presents several drawbacks and limitations. One primary disadvantage is the slow cooling process typically employed, which leads to a relatively slow crystal growth rate. As a result, the growth of large single crystals can be time-consuming, potentially increasing production costs. Additionally, although the method allows for precise temperature gradient control, maintaining a stable gradient remains challenging due to factors such as heat conduction, convection, and other operational variables. Furthermore, the Bridgman method may not be suitable for materials with a high thermal expansion coefficient or those prone to volatility. Notably, for materials that require extremely fine structural control, the Bridgman method may lack the necessary precision.

In summary, the Bridgman method for single crystal growth is poised to facilitate the advancement of larger, higher-quality, and higher-performance halide single crystals in future research. This progress will offer substantial support for the application of novel optoelectronic materials, semiconductor materials, and other functional materials. As the process continues to be refined, the Bridgman method will play an increasingly pivotal role in fields such as materials science, energy, and electronic devices.

Funding: This research was funded by Shandong Provincial Natural Science Foundation, grant number ZR2024QE319.

Data Availability Statement: No new data were created or analyzed in this study. Data sharing is not applicable to this article.

Acknowledgments: We would like to express our sincere gratitude to Zhiyan Zhou from the School of Stomatology, Shandong University, for her invaluable assistance with language polishing.

Conflicts of Interest: The authors declare no conflicts of interest.

References

1. Bisson, P.; Groenzin, H.; Barnett, I.L.; Shultz, M.J. High Yield, Single Crystal Ice via the Bridgman Method. *Rev. Sci. Instrum.* **2016**, *87*, 034103. [CrossRef] [PubMed]
2. Derby, J.J.; Yeckel, A. Heat Transfer Analysis and Design for Bulk Crystal Growth: Perspectives on the Bridgman Method. In *Handbook of Crystal Growth*; Elsevier: Amsterdam, The Netherlands, 2015; pp. 793–843, ISBN 978-0-444-63303-3.
3. Rudolph, P.; Kiessling, F. The Horizontal Bridgman Method. *Cryst. Res. Technol.* **1988**, *23*, 1207–1224. [CrossRef]
4. Gaxandet, J.P.; Alboussire, T. Bridgman Growth: Modelling and Experiments. *Prog. Cryst. Growth Charact. Mater.* **1999**, *38*, 133–159. [CrossRef]
5. Murugesan, M.; Sidden, C.; Paulraj, R. Growth, Optical and Thermal Properties of Triphenylamine Single Crystal Grown by Modified Vertical Bridgman Method for Optical Application. *Solid. State Sci.* **2022**, *132*, 106991. [CrossRef]
6. Fedyushkin, A.I.; Burago, N.G.; Puntus, A.A. Convective Heat and Mass Transfer Modeling under Crystal Growth by Vertical Bridgman Method. *J. Phys. Conf. Ser.* **2020**, *1479*, 012029. [CrossRef]
7. Yu, P.; Jiang, B.; Chen, Y.; Zheng, J.; Luan, L. Study on In-Doped CdMgTe Crystals Grown by a Modified Vertical Bridgman Method Using the ACRT Technique. *Materials* **2019**, *12*, 4236. [CrossRef] [PubMed]
8. Zhang, P.; Hua, Y.; Li, X.; Zhang, L.; Liu, L.; Li, R.; Zhang, G.; Tao, X. Filter-Free Color Image Sensor Based on $CsPbBr_{3-3n}$ X_{3n} (X = Cl, I) Single Crystals. *J. Mater. Chem. C* **2021**, *9*, 2840–2847. [CrossRef]
9. Gille, P.; Mühlberg, M.; Parthier, L.; Rudolph, P. Crystal Growth of PbTe and (Pb, Sn)Te by the Bridgman Method and by THM. *Cryst. Res. Technol.* **1984**, *19*, 881–891. [CrossRef]
10. Zhang, G.; Tao, X.; Wang, S.; Shi, Q.; Ruan, H.; Chen, L. Growth Improvement and Quality Evaluation of $ZnGeP_2$ Single Crystals Using Vertical Bridgman Method. *J. Cryst. Growth* **2012**, *352*, 67–71. [CrossRef]
11. Wang, C.; Xia, H.; Feng, Z.; Zhang, Z.; Jiang, D.; Gu, X.; Zhang, Y.; Chen, B.; Jiang, H. Infrared Luminescent Properties of $Na_5Lu_9F_{32}$ Single Crystals Co-Doped Er^{3+}/Yb^{3+} Grown by Bridgman Method. *J. Alloys Compd.* **2016**, *686*, 816–822. [CrossRef]
12. Mooney, R.P.; McFadden, S.; Gabalcová, Z.; Lapin, J. An Experimental–Numerical Method for Estimating Heat Transfer in a Bridgman Furnace. *Appl. Therm. Eng.* **2014**, *67*, 61–71. [CrossRef]
13. He, X.; Li, L.; He, X.; Xie, C. Multi-Physical Field Simulation of Cracking during Crystal Growth by Bridgman Method. *Materials* **2023**, *16*, 3260. [CrossRef] [PubMed]
14. Du, Y.; Jie, W.; Wang, T.; Zheng, X.; Xu, Y.; Luan, L. Solution Growth of In-Doped CdMnTe Crystals by the Vertical Bridgman Method with the ACRT Technique. *J. Cryst. Growth* **2012**, *355*, 33–37. [CrossRef]
15. Sheng, M.; Wang, S.; Zhu, H.; Liu, Z.; Zhou, G. Computational Applications for the Discovery of Novel Antiperovskites and Chalcogenide Perovskites: A Review. *Front. Chem.* **2024**, *12*, 1468434. [CrossRef] [PubMed]
16. Sheng, M.; Zhu, H.; Wang, S.; Liu, Z.; Zhou, G. Accelerated Discovery of Halide Perovskite Materials via Computational Methods: A Review. *Nanomaterials* **2024**, *14*, 1167. [CrossRef] [PubMed]
17. Wojakowska, A.; Krzy, E. Phase Diagram for the RbBr–CuBr System. *J. Therm. Anal. Calorim.* **2011**, *65*, 491–495. [CrossRef]
18. Kanno, R.; Takeda, Y.; Masuyama, Y.; Yamamoto, O. Phase Diagram and High Copper Ion Conductivity of the Copper(l) Chloride-Rubidium Chloride System. *Solid State Ion.* **1983**, *11*, 221–226. [CrossRef]
19. Takahashi, T. Solid-State Ionics—The CuCI-CuI-RbCl System. *Solid State Ion.* **1981**, *3*, 283–287. [CrossRef]
20. Malakhovskaya-Rosokha, T.A.; Barchii, I.E.; Pogodin, A.I.; Kokhan, A.P.; Stercho, I.P.; Peresh, E.Y. Interaction of Components in the RbI-CsI-CuI Quasi-Ternary System. *Russ. J. Inorg. Chem.* **2013**, *58*, 577–580. [CrossRef]
21. Matsui, T.; Wagner, J.B. Investigations on a High Conductivity Solid Electrolyte System, RbCl + CuCl. *J. Electrochem. Soc.* **1977**, *124*, 941–944. [CrossRef]
22. Gut, R.; Iberson, E.; Gruen, D.M. *Compounds in the Binary Phase Diagrams of the Monovalent Chlorides with the Multivalent Chlorides*; Report number ANL-6803; OSTI ID: 4117130; Argonne National Laboratory: Lemont, IL, USA, 1963.
23. Zhang, P.; Zhang, G.; Liu, L.; Ju, D.; Zhang, L.; Cheng, K.; Tao, X. Anisotropic Optoelectronic Properties of Melt-Grown Bulk $CsPbBr_3$ Single Crystal. *J. Phys. Chem. Lett.* **2018**, *9*, 5040–5046. [CrossRef] [PubMed]

24. Yu, X.; Huang, C.; Ni, Y.; Wang, Z.; Wu, H.; Hu, Q.; Liu, G.; Zhou, Q.; Wei, L. Optical Property and Judd-Ofelt Analysis of Dy^{3+}, Na+:$PbGa_2S_4$ Crystal Grown by Bridgman Method. *J. Lumin.* **2023**, *262*, 119951. [CrossRef]
25. Wang, L.-H.; Chang, L.-S. Thermoelectric Properties of P-Type $Ba_8Ga_{16}Ge_{30}$ Type-I Clathrate Compounds Prepared by the Vertical Bridgman Method. *J. Alloys Compd.* **2017**, *722*, 644–650. [CrossRef]
26. Zayachuk, D.M.; Ilyina, O.S.; Pashuk, A.V.; Mikityuk, V.I.; Shlemkevych, V.V.; Csik, A.; Kaczorowski, D. Segregation of the Eu Impurity as Function of Its Concentration in the Melt for Growing of the Lead Telluride Doped Crystals by the Bridgman Method. *J. Cryst. Growth* **2013**, *376*, 28–34. [CrossRef]
27. Lai, J.; Zhang, J.; Wang, L.; Min, J.; Wu, W.; Shen, M.; Liang, W. Comparison of Cadmium Manganese Telluride Crystals Grown by Traveling Heater Method and Vertical Bridgman Method. *Cryst. Res. Technol.* **2015**, *50*, 817–822. [CrossRef]
28. Xiong, W.; Chen, L.; Huang, L.; Guo, F.; Zhou, Y.; Yuan, H. Bridgman Growth and Characterization of Birefringent Crystal $NaNO_3$. *Cryst. Res. Technol.* **2015**, *50*, 250–254. [CrossRef]
29. Jin, M.; Shen, H.; Fan, S.; He, Q.; Xu, J. Industrial Growth and Characterization of Si-doped GaAs Crystal by a Novel Multi-crucible Bridgman Method. *Cryst. Res. Technol.* **2017**, *52*, 1700052. [CrossRef]
30. Yang, C.; Wen, Y.; Xiong, J.; Zhou, H.; Pan, S.; Chen, H.; Pan, J. Crystal Growth and Photoelectric Performance of γ-CuCl by the Vertical Bridgman Method. *J. Cryst. Growth* **2022**, *579*, 126463. [CrossRef]
31. Gul, R.; Roy, U.N.; Camarda, G.S.; Hossain, A.; Yang, G.; Vanier, P.; Lordi, V.; Varley, J.; James, R.B. A Comparison of Point Defects in $Cd_{1-x}Zn_xTe_{1-y}Sey$ Crystals Grown by Bridgman and Traveling Heater Methods. *J. Appl. Phys.* **2017**, *121*, 125705. [CrossRef]
32. Roy, U.N.; Bolotnikov, A.E.; Camarda, G.S.; Cui, Y.; Hossain, A.; Lee, K.; Lee, W.; Tappero, R.; Yang, G.; Gul, R.; et al. High Compositional Homogeneity of $CdTeSe_{1-x}$ Crystals Grown by the Bridgman Method. *APL Mater.* **2015**, *3*, 026102. [CrossRef]
33. Colombier, E.; Braithwaite, D. Simple Adaptation of the Bridgman High Pressure Technique for Use with Liquid Media. *Rev. Sci. Instrum.* **2007**, *78*, 093903. [CrossRef] [PubMed]
34. Li, L.; Zhang, P.; Li, Z.; Chen, Z. Thermal Field Simulation and Optimization of PbF_2 Single Crystal Growth by the Bridgman Method. *Crystals* **2024**, *14*, 473. [CrossRef]
35. Zhou, H.; Chen, X.; Zhao, T.; Chen, C.; Han, J.; Pan, S.; Pan, J. Growth and Luminescence Properties of γ-CuBr Single Crystals by the Bridgman Method. *CrystEngComm* **2023**, *25*, 1669–1674. [CrossRef]
36. Zayachuk, D.M.; Mikityuk, V.I.; Shlemkevych, V.V.; Kaczorowski, D. Complex Formation and Background Impurity of Oxygen in the PbTe: Eu Doped Crystals Grown from Melt by the Bridgman Method. *J. Cryst. Growth* **2012**, *338*, 35–41. [CrossRef]
37. Toufanian, R.; Swain, S.; Becla, P.; Motakef, S.; Datta, A. Cesium Lead Bromide Semiconductor Radiation Detectors: Crystal Growth, Detector Performance and Polarization. *J. Mater. Chem. C* **2022**, *10*, 12708–12714. [CrossRef]
38. Dahlen, A.; Fattah, A.; Hanke, G.; Karthaus, E. Bridgman and Czochralski Growth of Ge Si Alloy Crystals. *Cryst. Res. Technol.* **1994**, *29*, 187–198. [CrossRef]
39. Kliemt, K.; Krellner, C. Crystal Growth by Bridgman and Czochralski Method of the Ferromagnetic Quantum Critical Material $YbNi_4P_2$. *J. Cryst. Growth* **2016**, *449*, 129–133. [CrossRef]
40. Hurle, D.T.J. A Mechanism for Twin Formation during Czochralski and Encapsulated Vertical Bridgman Growth of III–V Compound Semiconductors. *J. Cryst. Growth* **1995**, *147*, 239–250. [CrossRef]
41. Tonn, J.; Danilewsky, A.N.; Cröll, A.; Matuchova, M.; Maixner, J. Czochralski Growth of Lead Iodide Single Crystals: Investigations and Comparison with the Bridgman Method. *J. Cryst. Growth* **2011**, *318*, 558–562. [CrossRef]
42. Akasaka, M.; Iida, T.; Matsumoto, A.; Yamanaka, K.; Takanashi, Y.; Imai, T.; Hamada, N. The Thermoelectric Properties of Bulk Crystalline N- and p-Type Mg_2Si Prepared by the Vertical Bridgman Method. *J. Appl. Phys.* **2008**, *104*, 013703. [CrossRef]
43. Lyubimova, T.P.; Croell, A.; Dold, P.; Khlybov, O.A.; Fayzrakhmanova, I.S. Time-Dependent Magnetic Field Influence on GaAs Crystal Growth by Vertical Bridgman Method. *J. Cryst. Growth* **2004**, *266*, 404–410. [CrossRef]
44. Shimizu, A.; Nishizawa, J.; Oyama, Y.; Suto, K. InP Single Crystal Growth by the Horizontal Bridgman Method under Controlled Phosphorus Vapor Pressure. *J. Cryst. Growth* **2001**, *229*, 119–123. [CrossRef]
45. Li, F.; Cabral, M.J.; Xu, B.; Cheng, Z.; Dickey, E.C.; LeBeau, J.M.; Wang, J.; Luo, J.; Taylor, S.; Hackenberger, W.; et al. Giant Piezoelectricity of Sm-Doped $Pb(Mg_{1/3}Nb_{2/3})O_3$-$PbTiO_3$ Single Crystals. *Science* **2019**, *364*, 264–268. [CrossRef]
46. Li, F.; Lin, D.; Chen, Z.; Cheng, Z.; Wang, J.; Li, C.; Xu, Z.; Huang, Q.; Liao, X.; Chen, L.-Q.; et al. Ultrahigh Piezoelectricity in Ferroelectric Ceramics by Design. *Nat. Mater.* **2018**, *17*, 349–354. [CrossRef]
47. Qiu, C.; Wang, B.; Zhang, N.; Zhang, S.; Liu, J.; Walker, D.; Wang, Y.; Tian, H.; Shrout, T.R.; Xu, Z.; et al. Transparent Ferroelectric Crystals with Ultrahigh Piezoelectricity. *Nature* **2020**, *577*, 350–354. [CrossRef] [PubMed]
48. Chen, H.; Liang, Z.; Luo, L.; Ke, Y.; Shen, Q.; Xia, Z.; Jiang, C.; Pan, J. Bridgman Growth, Crystallographic Characterization and Electrical Properties of Relaxor-Based Ferroelectric Single Crystal PIMNT. *J. Alloys Compd.* **2012**, *518*, 63–67. [CrossRef]
49. Liao, F.; Zhao, Y.; Chen, Z.; Zheng, Y.; Chen, H. Bridgman Growth and Photoelectronic Property of Relaxor-Based Ferroelectric Single Crystal $Pb(Sm_{1/2}Nb_{1/2})O_3$-$Pb(Mg_{1/3}Nb_{2/3})O_3$-$PbTiO_3$. *Crystals* **2021**, *11*, 402. [CrossRef]

50. Liu, Z.; Qin, X.; Liu, X. Luminescence Enrichment in Perovskite-Lanthanide Composites: Complexity and Complementarity. In *Handbook on the Physics and Chemistry of Rare Earths*; Elsevier: Amsterdam, The Netherlands, 2022; Volume 61, pp. 1–29, ISBN 978-0-323-98594-9.
51. Liu, Z.; Qin, X.; Chen, Q.; Jiang, T.; Chen, Q.; Liu, X. Metal–Halide Perovskite Nanocrystal Superlattice: Self-Assembly and Optical Fingerprints. *Adv. Mater.* **2023**, *35*, 2209279. [CrossRef] [PubMed]
52. Chen, Q.; Wu, J.; Ou, X.; Huang, B.; Almutlaq, J.; Zhumekenov, A.A.; Guan, X.; Han, S.; Liang, L.; Yi, Z.; et al. All-Inorganic Perovskite Nanocrystal Scintillators. *Nature* **2018**, *561*, 88–93. [CrossRef] [PubMed]
53. Liu, Z.; Qin, X.; Chen, Q.; Chen, Q.; Jing, Y.; Zhou, Z.; Zhao, Y.S.; Chen, J.; Liu, X. Highly Stable Lead-Free Perovskite Single Crystals with NIR Emission Beyond 1100 Nm. *Adv. Opt. Mater.* **2022**, *10*, 2201254. [CrossRef]
54. Ma, W.; Qian, Q.; Qaid, S.M.H.; Zhao, S.; Liang, D.; Cai, W.; Zang, Z. Water-Molecule-Induced Reversible Fluorescence in a One-Dimensional Mn-Based Hybrid Halide for Anticounterfeiting and Digital Encryption–Decryption. *Nano Lett.* **2023**, *23*, 8932–8939. [CrossRef]
55. Han, T.; Tan, S.; Xue, J.; Meng, L.; Lee, J.; Yang, Y. Interface and Defect Engineering for Metal Halide Perovskite Optoelectronic Devices. *Adv. Mater.* **2019**, *31*, 1803515. [CrossRef]
56. Motti, S.G.; Meggiolaro, D.; Martani, S.; Sorrentino, R.; Barker, A.J.; De Angelis, F.; Petrozza, A. Defect Activity in Lead Halide Perovskites. *Adv. Mater.* **2019**, *31*, 1901183. [CrossRef]
57. Ono, L.K.; Liu, S.; Qi, Y. Reducing Detrimental Defects for High-Performance Metal Halide Perovskite Solar Cells. *Angew. Chem. Int. Ed.* **2020**, *59*, 6676–6698. [CrossRef] [PubMed]
58. Huang, H.; Bodnarchuk, M.I.; Kershaw, S.V.; Kovalenko, M.V.; Rogach, A.L. Lead Halide Perovskite Nanocrystals in the Research Spotlight: Stability and Defect Tolerance. *ACS Energy Lett.* **2017**, *2*, 2071–2083. [CrossRef]
59. Yang, F.; Jie, W.; Wang, M.; Sun, X.; Jia, N.; Yin, L.; Zhou, B.; Wang, T. Growth of Single-Crystal Cd0.9Zn0.1Te Ingots Using Pressure Controlled Bridgman Method. *Crystals* **2020**, *10*, 261. [CrossRef]
60. Macpherson, S.; Doherty, T.A.S.; Winchester, A.J.; Kosar, S.; Johnstone, D.N.; Chiang, Y.-H.; Galkowski, K.; Anaya, M.; Frohna, K.; Iqbal, A.N.; et al. Local Nanoscale Phase Impurities Are Degradation Sites in Halide Perovskites. *Nature* **2022**, *607*, 294–300. [CrossRef] [PubMed]
61. Valueva, A.D.; Novikov, S.A.; Bledsoe, J.; Cai, Y.; Maksimova, A.A.; Locklin, J.; Zhao, Y.; Klepov, V.V. Cubic Halide Perovskites in the Cs(Pb_{1-x}Snx)($Br_{3-y}Cl_y$) Solid Solutions for Crack-Free Bridgman Grown Single Crystals. *MRS Commun.* **2024**, *14*, 942–948. [CrossRef]
62. Shi, Y.; Zhou, Y.; Ma, Z.; Xiao, G.; Wang, K.; Zou, B. Structural Regulation and Optical Behavior of Three-Dimensional Metal Halide Perovskites under Pressure. *J. Mater. Chem. C* **2020**, *8*, 12755–12767. [CrossRef]
63. Wong, W.P.D.; Yin, J.; Chaudhary, B.; Chin, X.Y.; Cortecchia, D.; Lo, S.-Z.A.; Grimsdale, A.C.; Mohammed, O.F.; Lanzani, G.; Soci, C. Large Polaron Self-Trapped States in Three-Dimensional Metal-Halide Perovskites. *ACS Mater. Lett.* **2020**, *2*, 20–27. [CrossRef]
64. Huang, X.; Guo, Q.; Kang, S.; Ouyang, T.; Chen, Q.; Liu, X.; Xia, Z.; Yang, Z.; Zhang, Q.; Qiu, J.; et al. Three-Dimensional Laser-Assisted Patterning of Blue-Emissive Metal Halide Perovskite Nanocrystals inside a Glass with Switchable Photoluminescence. *ACS Nano* **2020**, *14*, 3150–3158. [CrossRef] [PubMed]
65. Giappa, R.M.; Selivanov, N.I.; Samsonova, A.Y.; Pantousas, A.; Remediakis, I.N.; Kapitonov, Y.V.; Emeline, A.V.; Kopidakis, G.; Stoumpos, C.C. (3-CF_3pyH)$_2$(3-CF_3P_y)Pb_3I_8: A Three-Dimensional Metal Halide Inorganic Framework with Distinctive Kagomé Bands. *Chem. Mater.* **2024**, *36*, 11804–11813. [CrossRef]
66. Krawczyk, R.P.; Hammerl, A.; Schwerdtfeger, P. Coinage Metal Halide Clusters: From Two-Dimensional Ring to Three-Dimensional Solid-State-Like Structures. *ChemPhysChem* **2006**, *7*, 2286–2289. [CrossRef]
67. Zhang, W.; Eperon, G.E.; Snaith, H.J. Metal Halide Perovskites for Energy Applications. *Nat Energy* **2016**, *1*, 16048. [CrossRef]
68. Lei, L.; Dong, Q.; Gundogdu, K.; So, F. Metal Halide Perovskites for Laser Applications. *Adv Funct Mater.* **2021**, *31*, 2010144. [CrossRef]
69. Fu, Y.; Zhu, H.; Chen, J.; Hautzinger, M.P.; Zhu, X.-Y.; Jin, S. Metal Halide Perovskite Nanostructures for Optoelectronic Applications and the Study of Physical Properties. *Nat. Rev. Mater.* **2019**, *4*, 169–188. [CrossRef]
70. Stranks, S.D.; Snaith, H.J. Metal-Halide Perovskites for Photovoltaic and Light-Emitting Devices. *Nat. Nanotechnol.* **2015**, *10*, 391–402. [CrossRef] [PubMed]
71. Lin, Y.; Pattanasattayavong, P.; Anthopoulos, T.D. Metal-Halide Perovskite Transistors for Printed Electronics: Challenges and Opportunities. *Adv. Mater.* **2017**, *29*, 1702838. [CrossRef]
72. Sun, J.; Wu, J.; Tong, X.; Lin, F.; Wang, Y.; Wang, Z.M. Organic/Inorganic Metal Halide Perovskite Optoelectronic Devices beyond Solar Cells. *Adv. Sci.* **2018**, *5*, 1700780. [CrossRef] [PubMed]
73. Liu, X.-K.; Xu, W.; Bai, S.; Jin, Y.; Wang, J.; Friend, R.H.; Gao, F. Metal Halide Perovskites for Light-Emitting Diodes. *Nat. Mater.* **2021**, *20*, 10–21. [CrossRef] [PubMed]
74. Xiang, W.; Liu, S.; Tress, W. A Review on the Stability of Inorganic Metal Halide Perovskites: Challenges and Opportunities for Stable Solar Cells. *Energy Environ. Sci.* **2021**, *14*, 2090–2113. [CrossRef]

75. Cho, H.; Kim, Y.; Wolf, C.; Lee, H.; Lee, T. Improving the Stability of Metal Halide Perovskite Materials and Light-Emitting Diodes. *Adv. Mater.* **2018**, *30*, 1704587. [CrossRef]
76. Chen, X.; Wang, Y.; Song, J.; Li, X.; Xu, J.; Zeng, H.; Sun, H. Temperature Dependent Reflectance and Ellipsometry Studies on a $CsPbBr_3$ Single Crystal. *J. Phys. Chem. C* **2019**, *123*, 10564–10570. [CrossRef]
77. Cockroft, N.J.; Jones, G.D.; Nguyen, D.C. Dynamics and Spectroscopy of Infrared-to-Visible Upconversion in Erbium-Doped Cesium Cadmium Bromide ($CsCdBr_3$:Er^{3+}). *Phys. Rev. B* **1992**, *45*, 5187–5198. [CrossRef] [PubMed]
78. Pilla, O.; Cazzanelli, E.; Blanzat, B.; Andraud, C.; Pelle, F. Comparative Raman Study of Phonon Linewidths in Pure and Lead-Doped $CsCdBr_3$. *Phys. Status Solidi (B)* **1987**, *144*, 845–851. [CrossRef]
79. Stoumpos, C.C.; Malliakas, C.D.; Peters, J.A.; Liu, Z.; Sebastian, M.; Im, J.; Chasapis, T.C.; Wibowo, A.C.; Chung, D.Y.; Freeman, A.J.; et al. Crystal Growth of the Perovskite Semiconductor $CsPbBr_3$: A New Material for High-Energy Radiation Detection. *Cryst. Growth Des.* **2013**, *13*, 2722–2727. [CrossRef]
80. He, Y.; Matei, L.; Jung, H.J.; McCall, K.M.; Chen, M.; Stoumpos, C.C.; Liu, Z.; Peters, J.A.; Chung, D.Y.; Wessels, B.W.; et al. High Spectral Resolution of Gamma-Rays at Room Temperature by Perovskite $CsPbBr_3$ Single Crystals. *Nat. Commun.* **2018**, *9*, 1609. [CrossRef] [PubMed]
81. Dirin, D.N.; Cherniukh, I.; Yakunin, S.; Shynkarenko, Y.; Kovalenko, M.V. Solution-Grown $CsPbBr_3$ Perovskite Single Crystals for Photon Detection. *Chem. Mater.* **2016**, *28*, 8470–8474. [CrossRef] [PubMed]
82. Liu, D.; Hu, Z.; Hu, W.; Wangyang, P.; Yu, K.; Wen, M.; Zu, Z.; Liu, J.; Wang, M.; Chen, W.; et al. Two-Step Method for Preparing All-Inorganic $CsPbBr_3$ Perovskite Film and Its Photoelectric Detection Application. *Mater. Lett.* **2017**, *186*, 243–246. [CrossRef]
83. Tang, X.; Zu, Z.; Zang, Z.; Hu, Z.; Hu, W.; Yao, Z.; Chen, W.; Li, S.; Han, S.; Zhou, M. $CsPbBr_3$/Reduced Graphene Oxide Nanocomposites and Their Enhanced Photoelectric Detection Application. *Sens. Actuators B Chem.* **2017**, *245*, 435–440. [CrossRef]
84. Adinolfi, V.; Yuan, M.; Comin, R.; Thibau, E.S.; Shi, D.; Saidaminov, M.I.; Kanjanaboos, P.; Kopilovic, D.; Hoogland, S.; Lu, Z.; et al. The In-Gap Electronic State Spectrum of Methylammonium Lead Iodide Single-Crystal Perovskites. *Adv. Mater.* **2016**, *28*, 3406–3410. [CrossRef] [PubMed]
85. Kang, J.; Wang, L.-W. High Defect Tolerance in Lead Halide Perovskite $CsPbBr_3$. *J. Phys. Chem. Lett.* **2017**, *8*, 489–493. [CrossRef] [PubMed]
86. Chen, C.; Fu, Q.; Guo, P.; Chen, H.; Wang, M.; Luo, W.; Zheng, Z. Ionic Transport Characteristics of Large-Size $CsPbBr_3$ Single Crystals. *Mater. Res. Express* **2019**, *6*, 115808. [CrossRef]
87. Li, J.; Du, X.; Niu, G.; Xie, H.; Chen, Y.; Yuan, Y.; Gao, Y.; Xiao, H.; Tang, J.; Pan, A.; et al. Rubidium Doping to Enhance Carrier Transport in $CsPbBr_3$ Single Crystals for High-Performance X-Ray Detection. *ACS Appl. Mater. Interfaces* **2020**, *12*, 989–996. [CrossRef]
88. Lee, I.Y.; Deleplanque, M.A.; Vetter, K. Developments in Large Gamma-Ray Detector Arrays. *Rep. Prog. Phys.* **2003**, *66*, 1095–1144. [CrossRef]
89. Liu, H.; Omura, T.; Watanabe, M.; Yamashita, T. Development of a Depth of Interaction Detector for γ-Rays. *Nucl. Instrum. Methods Phys. Res. Sect. A Accel. Spectrometers Detect. Assoc. Equip.* **2001**, *459*, 182–190. [CrossRef]
90. Funk, S. Indirect Detection of Dark Matter with γ Rays. *Proc. Natl. Acad. Sci. USA* **2015**, *112*, 12264–12271. [CrossRef] [PubMed]
91. Xu, J.; Maxwell, A.; Wei, M.; Wang, Z.; Chen, B.; Zhu, T.; Sargent, E.H. Defect Tolerance of Mixed B-Site Organic–Inorganic Halide Perovskites. *ACS Energy Lett.* **2021**, *6*, 4220–4227. [CrossRef]
92. Smart, T.J.; Takenaka, H.; Pham, T.A.; Tan, L.Z.; Zhang, J.Z.; Ogitsu, T.; Ping, Y. Enhancing Defect Tolerance with Ligands at the Surface of Lead Halide Perovskites. *J. Phys. Chem. Lett.* **2021**, *12*, 6299–6304. [CrossRef] [PubMed]
93. Kim, G.; Petrozza, A. Defect Tolerance and Intolerance in Metal-Halide Perovskites. *Adv. Energy Mater.* **2020**, *10*, 2001959. [CrossRef]
94. He, Y.; Stoumpos, C.C.; Hadar, I.; Luo, Z.; McCall, K.M.; Liu, Z.; Chung, D.Y.; Wessels, B.W.; Kanatzidis, M.G. Demonstration of Energy-Resolved γ-Ray Detection at Room Temperature by the $CsPbCl_3$ Perovskite Semiconductor. *J. Am. Chem. Soc.* **2021**, *143*, 2068–2077. [CrossRef] [PubMed]
95. Cohen, M.I.; Young, K.F.; Chang, T.-T.; Brower, W.S. Phase Transitions in $CsPbCl_3$. *J. Appl. Phys.* **1971**, *42*, 5267–5272. [CrossRef]
96. Kobayashi, M.; Omata, K.; Sugimoto, S.; Tamagawa, Y.; Kuroiwa, T.; Asada, H.; Takeuchi, H.; Kondo, S. Scintillation Characteristics of $CsPbCl_3$ Single Crystals. *Nucl. Instrum. Methods Phys. Res. Sect. A Accel. Spectrometers Detect. Assoc. Equip.* **2008**, *592*, 369–373. [CrossRef]
97. Balvanz, A.; Bayikadi, K.S.; Liu, Z.; Ie, T.S.; Peters, J.A.; Kanatzidis, M.G. Unveiling the Monoclinic Phase in $CsPbBr_{3-x}Cl_x$ Perovskite Crystals, Phase Transition Suppression and High Energy Resolution γ-Ray Detection. *J. Am. Chem. Soc.* **2024**, *146*, 31836–31848. [CrossRef] [PubMed]
98. Liu, F.; Wu, R.; Wei, J.; Nie, W.; Mohite, A.D.; Brovelli, S.; Manna, L.; Li, H. Recent Progress in Halide Perovskite Radiation Detectors for Gamma-Ray Spectroscopy. *ACS Energy Lett.* **2022**, *7*, 1066–1085. [CrossRef]
99. Yoon, S.J.; Stamplecoskie, K.G.; Kamat, P.V. How Lead Halide Complex Chemistry Dictates the Composition of Mixed Halide Perovskites. *J. Phys. Chem. Lett.* **2016**, *7*, 1368–1373. [CrossRef] [PubMed]

100. Xiao, Z.; Zhao, L.; Tran, N.L.; Lin, Y.L.; Silver, S.H.; Kerner, R.A.; Yao, N.; Kahn, A.; Scholes, G.D.; Rand, B.P. Mixed-Halide Perovskites with Stabilized Bandgaps. *Nano Lett.* **2017**, *17*, 6863–6869. [CrossRef]
101. Knight, A.J.; Borchert, J.; Oliver, R.D.J.; Patel, J.B.; Radaelli, P.G.; Snaith, H.J.; Johnston, M.B.; Herz, L.M. Halide Segregation in Mixed-Halide Perovskites: Influence of A-Site Cations. *ACS Energy Lett.* **2021**, *6*, 799–808. [CrossRef]
102. Zarick, H.F.; Soetan, N.; Erwin, W.R.; Bardhan, R. Mixed Halide Hybrid Perovskites: A Paradigm Shift in Photovoltaics. *J. Mater. Chem. A* **2018**, *6*, 5507–5537. [CrossRef]
103. Nedelcu, G.; Protesescu, L.; Yakunin, S.; Bodnarchuk, M.I.; Grotevent, M.J.; Kovalenko, M.V. Fast Anion-Exchange in Highly Luminescent Nanocrystals of Cesium Lead Halide Perovskites ($CsPbX_3$, X = Cl, Br, I). *Nano Lett.* **2015**, *15*, 5635–5640. [CrossRef] [PubMed]
104. Yu, Y.; Zhang, D.; Yang, P. Ruddlesden–Popper Phase in Two-Dimensional Inorganic Halide Perovskites: A Plausible Model and the Supporting Observations. *Nano Lett.* **2017**, *17*, 5489–5494. [CrossRef]
105. Pan, D.; Fu, Y.; Spitha, N.; Zhao, Y.; Roy, C.R.; Morrow, D.J.; Kohler, D.D.; Wright, J.C.; Jin, S. Deterministic Fabrication of Arbitrary Vertical Heterostructures of Two-Dimensional Ruddlesden–Popper Halide Perovskites. *Nat. Nanotechnol.* **2021**, *16*, 159–165. [CrossRef] [PubMed]
106. Chen, Z.; Guo, Y.; Wertz, E.; Shi, J. Merits and Challenges of Ruddlesden–Popper Soft Halide Perovskites in Electro-Optics and Optoelectronics. *Adv. Mater.* **2019**, *31*, 1803514. [CrossRef] [PubMed]
107. Gong, J.; Hao, M.; Zhang, Y.; Liu, M.; Zhou, Y. Layered 2D Halide Perovskites beyond the Ruddlesden–Popper Phase: Tailored Interlayer Chemistries for High-Performance Solar Cells. *Angew. Chem.* **2022**, *134*, e202112022. [CrossRef]
108. Chen, Y.; Sun, Y.; Peng, J.; Tang, J.; Zheng, K.; Liang, Z. 2D Ruddlesden–Popper Perovskites for Optoelectronics. *Adv. Mater.* **2018**, *30*, 1703487. [CrossRef]
109. Li, J.; Yu, Q.; He, Y.; Stoumpos, C.C.; Niu, G.; Trimarchi, G.G.; Guo, H.; Dong, G.; Wang, D.; Wang, L.; et al. $Cs_2PbI_2Cl_2$, All-Inorganic Two-Dimensional Ruddlesden–Popper Mixed Halide Perovskite with Optoelectronic Response. *J. Am. Chem. Soc.* **2018**, *140*, 11085–11090. [CrossRef] [PubMed]
110. Ruddlesden, S.N.; Popper, P. New Compounds of the K_2NIF_4 Type. *Acta Cryst* **1957**, *10*, 538–539. [CrossRef]
111. Kresse, G.; Furthmüller, J. Efficiency of Ab-Initio Total Energy Calculations for Metals and Semiconductors Using a Plane-Wave Basis Set. *Comput. Mater. Sci.* **1996**, *6*, 15–50. [CrossRef]
112. Kresse, G.; Furthmüller, J. Efficient Iterative Schemes for Ab Initio Total-Energy Calculations Using a Plane-Wave Basis Set. *Phys. Rev. B* **1996**, *54*, 11169–11186. [CrossRef]
113. Acharyya, P.; Ghosh, T.; Pal, K.; Kundu, K.; Singh Rana, K.; Pandey, J.; Soni, A.; Waghmare, U.V.; Biswas, K. Intrinsically Ultralow Thermal Conductivity in Ruddlesden–Popper 2D Perovskite $Cs_2PbI_2Cl_2$: Localized Anharmonic Vibrations and Dynamic Octahedral Distortions. *J. Am. Chem. Soc.* **2020**, *142*, 15595–15603. [CrossRef] [PubMed]
114. Delaire, O.; Ma, J.; Marty, K.; May, A.F.; McGuire, M.A.; Du, M.-H.; Singh, D.J.; Podlesnyak, A.; Ehlers, G.; Lumsden, M.D.; et al. Giant Anharmonic Phonon Scattering in PbTe. *Nat. Mater.* **2011**, *10*, 614–619. [CrossRef] [PubMed]
115. Dissanayake, P.D.; Yeom, K.M.; Sarkar, B.; Alessi, D.S.; Hou, D.; Rinklebe, J.; Noh, J.H.; Ok, Y.S. Environmental Impact of Metal Halide Perovskite Solar Cells and Potential Mitigation Strategies: A Critical Review. *Environ. Res.* **2023**, *219*, 115066. [CrossRef]
116. Lyu, M.; Yun, J.; Chen, P.; Hao, M.; Wang, L. Addressing Toxicity of Lead: Progress and Applications of Low-Toxic Metal Halide Perovskites and Their Derivatives. *Adv. Energy Mater.* **2017**, *7*, 1602512. [CrossRef]
117. Xiao, Z.; Song, Z.; Yan, Y. From Lead Halide Perovskites to Lead-Free Metal Halide Perovskites and Perovskite Derivatives. *Adv. Mater.* **2019**, *31*, 1803792. [CrossRef]
118. Hu, H.; Dong, B.; Zhang, W. Low-Toxic Metal Halide Perovskites: Opportunities and Future Challenges. *J. Mater. Chem. A* **2017**, *5*, 11436–11449. [CrossRef]
119. De Souza Carvalho, T.A.; Magalhaes, L.F.; Do Livramento Santos, C.I.; De Freitas, T.A.Z.; Carvalho Vale, B.R.; Vale Da Fonseca, A.F.; Schiavon, M.A. Lead-Free Metal Halide Perovskite Nanocrystals: From Fundamentals to Applications. *Chem. Eur. J.* **2023**, *29*, e202202518. [CrossRef] [PubMed]
120. Zhang, L.; Wang, K.; Zou, B. Bismuth Halide Perovskite-Like Materials: Current Opportunities and Challenges. *ChemSusChem* **2019**, *12*, 1612–1630. [CrossRef]
121. Ayscue, R.L.; Vallet, V.; Bertke, J.A.; Réal, F.; Knope, K.E. Structure–Property Relationships in Photoluminescent Bismuth Halide Organic Hybrid Materials. *Inorg. Chem.* **2021**, *60*, 9727–9744. [CrossRef] [PubMed]
122. Creutz, S.E.; Liu, H.; Kaiser, M.E.; Li, X.; Gamelin, D.R. Structural Diversity in Cesium Bismuth Halide Nanocrystals. *Chem. Mater.* **2019**, *31*, 4685–4697. [CrossRef]
123. Li, X.; Du, X.; Zhang, P.; Hua, Y.; Liu, L.; Niu, G.; Zhang, G.; Tang, J.; Tao, X. Lead-Free Halide Perovskite $Cs_3Bi_2Br_9$ Single Crystals for High-Performance X-Ray Detection. *Sci. China Mater.* **2021**, *64*, 1427–1436. [CrossRef]
124. Leng, M.; Yang, Y.; Zeng, K.; Chen, Z.; Tan, Z.; Li, S.; Li, J.; Xu, B.; Li, D.; Hautzinger, M.P.; et al. All-Inorganic Bismuth-Based Perovskite Quantum Dots with Bright Blue Photoluminescence and Excellent Stability. *Adv. Funct. Mater.* **2018**, *28*, 1704446. [CrossRef]

125. Bass, K.K.; Estergreen, L.; Savory, C.N.; Buckeridge, J.; Scanlon, D.O.; Djurovich, P.I.; Bradforth, S.E.; Thompson, M.E.; Melot, B.C. Vibronic Structure in Room Temperature Photoluminescence of the Halide Perovskite $Cs_3Bi_2Br_9$. *Inorg. Chem.* **2017**, *56*, 42–45. [CrossRef]
126. Li, X.; Zhang, G.; Hua, Y.; Cui, F.; Sun, X.; Liu, J.; Liu, H.; Bi, Y.; Yue, Z.; Zhai, Z.; et al. Dimensional and Optoelectronic Tuning of Lead-free Perovskite $Cs_3Bi_2I_{9-n}Br_n$ Single Crystals for Enhanced Hard X-ray Detection. *Angew. Chem. Int. Ed.* **2023**, *62*, e202315817. [CrossRef] [PubMed]
127. Zhou, Y.; Fei, C.; Uddin, M.A.; Zhao, L.; Ni, Z.; Huang, J. Self-Powered Perovskite Photon-Counting Detectors. *Nature* **2023**, *616*, 712–718. [CrossRef] [PubMed]
128. Zhang, X.; Zhu, T.; Ji, C.; Yao, Y.; Luo, J. In Situ Epitaxial Growth of Centimeter-Sized Lead-Free $(BA)_2CsAgBiBr_7/Cs_2$ $AgBiBr_6$ Heterocrystals for Self-Driven X-Ray Detection. *J. Am. Chem. Soc.* **2021**, *143*, 20802–20810. [CrossRef]
129. McCall, K.M.; Stoumpos, C.C.; Kostina, S.S.; Kanatzidis, M.G.; Wessels, B.W. Strong Electron–Phonon Coupling and Self-Trapped Excitons in the Defect Halide Perovskites $A_3M_2I_9$ (A = Cs, Rb; M = Bi, Sb). *Chem. Mater.* **2017**, *29*, 4129–4145. [CrossRef]
130. McCall, K.M.; Liu, Z.; Trimarchi, G.; Stoumpos, C.C.; Lin, W.; He, Y.; Hadar, I.; Kanatzidis, M.G.; Wessels, B.W. α-Particle Detection and Charge Transport Characteristics in the $A_3M_2I_9$ Defect Perovskites (A = Cs, Rb; M = Bi, Sb). *ACS Photonics* **2018**, *5*, 3748–3762. [CrossRef]
131. Lei, X.-W.; Yue, C.-Y.; Zhao, J.-Q.; Han, Y.-F.; Yang, J.-T.; Meng, R.-R.; Gao, C.-S.; Ding, H.; Wang, C.-Y.; Chen, W.-D. Low-Dimensional Hybrid Cuprous Halides Directed by Transition Metal Complex: Syntheses, Crystal Structures, and Photocatalytic Properties. *Cryst. Growth Des.* **2015**, *15*, 5416–5426. [CrossRef]
132. Cheng, P.; Sun, L.; Feng, L.; Yang, S.; Yang, Y.; Zheng, D.; Zhao, Y.; Sang, Y.; Zhang, R.; Wei, D.; et al. Colloidal Synthesis and Optical Properties of All-Inorganic Low-Dimensional Cesium Copper Halide Nanocrystals. *Angew. Chem.* **2019**, *131*, 16233–16237. [CrossRef]
133. Zhang, P.; Yan, Z.; Li, C.; Du, Y.; Ma, L.; Wang, Z.; Lin, T.; Zhao, L.; Xiao, J. Low-Dimensional Hybrid Copper(I) Halides Single Crystals: Synthesis, Structures, and Tunable Photoluminescence. *Chem. Eng. J.* **2024**, *496*, 154106. [CrossRef]
134. Wang, Q.; Wang, C.; Wang, Z.; Sun, X.; Nikl, M.; OuYang, X.; Wu, Y. Achieving Efficient Neutron and Gamma Discrimination in a Highly Stable^6 Li-Loaded $Cs_3Cu_2I_5$ Perovskite Scintillator. *J. Phys. Chem. Lett.* **2022**, *13*, 9066–9071. [CrossRef] [PubMed]
135. Liu, D.; Wei, Q.; Tong, Y.; Xiang, P.; Cai, P.; Tang, G.; Shi, H.; Qin, L. A Novel Li^+-Doped $CsCu_2I_3$ Single Crystal for Dual Gamma–Neutron Detection. *CrystEngComm* **2023**, *25*, 58–63. [CrossRef]
136. Combes, C.M.; Dorenbos, P.; Van Eijk, C.W.E.; Krämer, K.W.; Güdel, H.U. Optical and Scintillation Properties of Pure and Ce^{3+}-Doped Cs_2LiYCl_6 and Li_3YCl_6:Ce^{3+} Crystals. *J. Lumin.* **1999**, *82*, 299–305. [CrossRef]
137. Glodo, J.; Hawrami, R.; Shah, K.S. Development of Cs_2LiYCl_6 Scintillator. *J. Cryst. Growth* **2013**, *379*, 73–78. [CrossRef]
138. Cheng, S.; Nikl, M.; Beitlerova, A.; Kucerkova, R.; Du, X.; Niu, G.; Jia, Y.; Tang, J.; Ren, G.; Wu, Y. Ultrabright and Highly Efficient All-Inorganic Zero-Dimensional Perovskite Scintillators. *Adv. Opt. Mater.* **2021**, *9*, 2100460. [CrossRef]
139. Wang, Q.; Zhou, Q.; Nikl, M.; Xiao, J.; Kucerkova, R.; Beitlerova, A.; Babin, V.; Prusa, P.; Linhart, V.; Wang, J.; et al. Highly Resolved X-Ray Imaging Enabled by In(I) Doped Perovskite-Like $Cs_3Cu_2I_5$ Single Crystal Scintillator. *Adv. Opt. Mater.* **2022**, *10*, 2200304. [CrossRef]
140. Belousov, M.P.; Gromyko, M.V.; Ignatyev, O.V. Scintillation γ Spectrometers for Use at Nuclear Power Plants (Review). *Instrum. Exp. Tech.* **2017**, *60*, 1–19. [CrossRef]
141. Dorenbos, P. (INVITED) The Quest for High Resolution γ-Ray Scintillators. *Opt. Mater. X* **2019**, *1*, 100021. [CrossRef]
142. Yuan, D. Air-Stable Bulk Halide Single-Crystal Scintillator $Cs_3Cu_2I_5$ by Melt Growth: Intrinsic and Tl Doped with High Light Yield. *ACS Appl. Mater. Interfaces* **2020**, *12*, 38333–38340. [CrossRef]
143. Tsuji, M.; Sasase, M.; Iimura, S.; Kim, J.; Hosono, H. Room-Temperature Solid-State Synthesis of $Cs_3Cu_2I_5$ Thin Films and Formation Mechanism for Its Unique Local Structure. *J. Am. Chem. Soc.* **2023**, *145*, 11650–11658. [CrossRef]
144. Wang, Z.; Wang, L.; Xie, J.; Yang, Y.; Song, Y.; Xiao, G.; Fu, Y.; Zhang, L.; Fang, Y.; Yang, D.; et al. $HCOO^-$ Doping-Induced Multiexciton Emissions in $Cs_3Cu_2I_5$ Crystals for Efficient X-Ray Scintillation. *Small* **2024**, *20*, 2309922. [CrossRef]
145. Chen, H.; Pina, J.M.; Yuan, F.; Johnston, A.; Ma, D.; Chen, B.; Li, Z.; Dumont, A.; Li, X.; Liu, Y.; et al. Multiple Self-Trapped Emissions in the Lead-Free Halide Cs_3 Cu_2 I_5. *J. Phys. Chem. Lett.* **2020**, *11*, 4326–4330. [CrossRef] [PubMed]
146. Lian, L.; Zheng, M.; Zhang, W.; Yin, L.; Du, X.; Zhang, P.; Zhang, X.; Gao, J.; Zhang, D.; Gao, L.; et al. Efficient and Reabsorption-Free Radioluminescence in $Cs_3Cu_2I_5$ Nanocrystals with Self-Trapped Excitons. *Adv. Sci.* **2020**, *7*, 2000195. [CrossRef] [PubMed]
147. Jun, T.; Sim, K.; Iimura, S.; Sasase, M.; Kamioka, H.; Kim, J.; Hosono, H. Lead-Free Highly Efficient Blue-Emitting $Cs_3Cu_2I_5$ with 0D Electronic Structure. *Adv. Mater.* **2018**, *30*, 1804547. [CrossRef]
148. Li, X.; Chen, J.; Yang, D.; Chen, X.; Geng, D.; Jiang, L.; Wu, Y.; Meng, C.; Zeng, H. Mn^{2+} Induced Significant Improvement and Robust Stability of Radioluminescence in $Cs_3Cu_2I_5$ for High-Performance Nuclear Battery. *Nat. Commun.* **2021**, *12*, 3879. [CrossRef] [PubMed]
149. Heo, J.H.; Shin, D.H.; Park, J.K.; Kim, D.H.; Lee, S.J.; Im, S.H. High-Performance Next-Generation Perovskite Nanocrystal Scintillator for Nondestructive X-Ray Imaging. *Adv. Mater.* **2018**, *30*, 1801743. [CrossRef]

150. Van Loef, E.V.; Ciampi, G.; Shirwadkar, U.; Soundara Pandian, L.; Shah, K.S. Crystal Growth and Scintillation Properties of Thallium-Based Halide Scintillators. *J. Cryst. Growth* **2020**, *532*, 125438. [CrossRef]
151. Shirwadkar, U.; Loyd, M.; Du, M.-H.; Van Loef, E.; Ciampi, G.; Soundara Pandian, L.; Stand, L.; Koschan, M.; Zhuravleva, M.; Melcher, C.; et al. Thallium-Based Scintillators for High-Resolution Gamma-Ray Spectroscopy: Ce^{3+}-Doped Tl_2LaCl_5 and Tl_2LaBr_5. *Nucl. Instrum. Methods Phys. Res. Sect. A Accel. Spectrometers Detect. Assoc. Equip.* **2020**, *962*, 163684. [CrossRef]
152. Hawrami, R.; Ariesanti, E.; Buliga, V.; Burger, A. Thallium Strontium Iodide: A High Efficiency Scintillator for Gamma-Ray Detection. *Opt. Mater.* **2020**, *100*, 109624. [CrossRef]
153. Kim, H.; Khan, A.; Daniel, J.; Rooh, G.; Vuong, P.Q. Thallium-Based Heavy Inorganic Scintillators: Recent Developments and Future Perspectives. *CrystEngComm* **2022**, *24*, 450–464. [CrossRef]
154. Pan, L.; Sholom, S.; McKeever, S.W.S.; Jacobsohn, L.G. Magnesium Aluminate Spinel for Optically Stimulated Luminescence Dosimetry. *J. Alloys Compd.* **2021**, *880*, 160503. [CrossRef]
155. Sakai, T.; Koshimizu, M.; Fujimoto, Y.; Nakauchi, D.; Yanagida, T.; Asai, K. Luminescence and Scintillation Properties of Tl- and In-Doped CsCl Crystals. *Jpn. J. Appl. Phys.* **2017**, *56*, 062601. [CrossRef]
156. Zazubovich, S.; Voloshinovskii, A.; Stryganyuk, G. Luminescence of CsCl: Tl Crystal under Synchrotron Excitation. *Phys. Status Solidi (B)* **2002**, *233*, 238–249. [CrossRef]
157. Nagirnyi, V.; Zazubovich, S.; Jaanson, N. Luminescence of CsCl: Tl Single Crystals. *Phys. Status Solidi (B)* **1993**, *175*, 155–164. [CrossRef]
158. Shiran, N.V.; Gektin, A.V.; Boyarintseva, Y.; Vasyukov, S.; Boyarintsev, A.; Pedash, V.; Tkachenko, S.; Zelenskaya, O.; Kosinov, N.; Kisil, O.; et al. Eu Doped and Eu, Tl Co-Doped NaI Scintillators. *IEEE Trans. Nucl. Sci.* **2010**, *57*, 1233–1235. [CrossRef]
159. Lin, W.; He, J.; McCall, K.M.; Stoumpos, C.C.; Liu, Z.; Hadar, I.; Das, S.; Wang, H.; Wang, B.; Chung, D.Y.; et al. Inorganic Halide Perovskitoid $TlPbI_3$ for Ionizing Radiation Detection. *Adv. Funct. Mater.* **2021**, *31*, 2006635. [CrossRef]
160. Rodi, F.; Babel, D. Ternäre Oxide der Übergangsmetalle. IV. Erdalkaliiridium(IV)-oxide: Kristallstruktur von $CalrO_3$. *Z. Anorg Allge Chem.* **1965**, *336*, 17–23. [CrossRef]
161. Li, X.; He, Y.; Kepenekian, M.; Guo, P.; Ke, W.; Even, J.; Katan, C.; Stoumpos, C.C.; Schaller, R.D.; Kanatzidis, M.G. Three-Dimensional Lead Iodide Perovskitoid Hybrids with High X-Ray Photoresponse. *J. Am. Chem. Soc.* **2020**, *142*, 6625–6637. [CrossRef]
162. Vtyurina, D.N.; Kaurova, I.A.; Kuz'micheva, G.M.; Rybakov, V.B.; Chernyshov, D.Y.; Khramov, E.V.; Firstov, S.V.; Korchak, V.N. Structural Peculiarities, Point Defects and Luminescence in Bi-Doped $CsCdX_3$ (X = Cl, Br) Single Crystals. *J. Alloys Compd.* **2019**, *803*, 912–921. [CrossRef]
163. Vtyurina, D.N.; Eistrikh-Geller, P.A.; Kuz'micheva, G.M.; Rybakov, V.B.; Khramov, E.V.; Kaurova, I.A.; Chernyshov, D.Y.; Korchak, V.N. Influence of Monovalent Bi+ Doping on Real Composition, Point Defects, and Photoluminescence in $TlCdCl_3$ and $TlCdI_3$ Single Crystals. *Sci. China Mater.* **2017**, *60*, 1253–1263. [CrossRef]
164. Yang, G.; Phan, Q.V.; Liu, M.; Hawari, A.; Kim, H. Material Defect Study of Thallium Lead Iodide ($TlPbI_3$) Crystals for Radiation Detector Applications. *Nucl. Instrum. Methods Phys. Res. Sect. A Accel. Spectrometers Detect. Assoc. Equip.* **2020**, *954*, 161516. [CrossRef]
165. Liu, Z.; Zhang, T.; Wang, Y.; Wang, C.; Zhang, P.; Sarvari, H.; Chen, Z.; Li, S. Electronic Properties of a New All-Inorganic Perovskite $TlPbI_3$ Simulated by the First Principles. *Nanoscale Res. Lett.* **2017**, *12*, 232. [CrossRef]
166. Yan, Y.; Liu, F.; Wu, J.; Zhang, Z.; Wu, Z.; Cong, W.-Y.; Guan, C.; Lu, Y.-B. Evaluation of the Electronic Properties of Layered $TlPbI_3$ Perovskites. *Phys. B Condens. Matter* **2023**, *667*, 415190. [CrossRef]
167. Khyzhun, O.Y.; Fochuk, P.M.; Kityk, I.V.; Piasecki, M.; Levkovets, S.I.; Fedorchuk, A.O.; Parasyuk, O.V. Single Crystal Growth and Electronic Structure of $TlPbI_3$. *Mater. Chem. Phys.* **2016**, *172*, 165–172. [CrossRef]
168. Lin, W.; Stoumpos, C.C.; Liu, Z.; Das, S.; Kontsevoi, O.Y.; He, Y.; Malliakas, C.D.; Chen, H.; Wessels, B.W.; Kanatzidis, M.G. $TlSn_2I_5$, a Robust Halide Antiperovskite Semiconductor for γ-Ray Detection at Room Temperature. *ACS Photonics* **2017**, *4*, 1805–1813. [CrossRef]
169. Li, W.; Li, M.; He, Y.; Song, J.; Guo, K.; Pan, W.; Wei, H. Arising 2D Perovskites for Ionizing Radiation Detection. *Adv. Mater.* **2024**, *36*, 2309588. [CrossRef] [PubMed]
170. Ni, Z.; Zhao, J.; Zhang, G.; Chen, Y.; Lian, H.; Lin, J. Synthesis of Pb-free Double-Perovskite Heterojunction (Cs_2SnCl_6-Bi^{3+}&Te^{4+}/Cs_2GeF_6-Mn^{4+}) with White Emission for LED Application. *Adv. Opt. Mater.* **2023**, *11*, 2203029. [CrossRef]
171. Zhou, J.; Luo, J.; Rong, X.; Wei, P.; Molokeev, M.S.; Huang, Y.; Zhao, J.; Liu, Q.; Zhang, X.; Tang, J.; et al. Lead-Free Perovskite Derivative Cs_2 $SnCl_{6-x}Br_x$Single Crystals for Narrowband Photodetectors. *Adv. Opt. Mater.* **2019**, *7*, 1900139. [CrossRef]
172. Sun, J.; Zheng, W.; Huang, P.; Zhang, M.; Zhang, W.; Deng, Z.; Yu, S.; Jin, M.; Chen, X. Efficient Near-Infrared Luminescence in Lanthanide-Doped Vacancy-Ordered Double Perovskite Cs_2ZrCl_6 Phosphors via Te^{4+} Sensitization. *Angew. Chem. Int. Ed.* **2022**, *61*, e202201993. [CrossRef]
173. Wang, A.; Yan, X.; Zhang, M.; Sun, S.; Yang, M.; Shen, W.; Pan, X.; Wang, P.; Deng, Z. Controlled Synthesis of Lead-Free and Stable Perovskite Derivative Cs_2SnI_6 Nanocrystals via a Facile Hot-Injection Process. *Chem. Mater.* **2016**, *28*, 8132–8140. [CrossRef]

174. Scott, S.M.; Zhu, W.; Yao, T.; Vienna, J.D.; Ewing, R.C.; Lian, J. The Thermal Stability and Consolidation of Perovskite Variant Cs_2SnCl_6 Using Spark Plasma Sintering. *J. Am. Ceram. Soc.* **2018**, *101*, 2060–2065. [CrossRef]
175. Chang, T.; Wei, Q.; Zeng, R.; Cao, S.; Zhao, J.; Zou, B. Efficient Energy Transfer in Te^{4+}-Doped Cs_2ZrCl_6 Vacancy-Ordered Perovskites and Ultrahigh Moisture Stability via A-Site Rb-Alloying Strategy. *J. Phys. Chem. Lett.* **2021**, *12*, 1829–1837. [CrossRef] [PubMed]
176. Qing, X.; Wu, C.; Han, X. Efficient Near-Infrared Luminescence Based on Double Perovskite Cs_2SnCl_6. *Molecules* **2023**, *28*, 3593. [CrossRef] [PubMed]
177. Jin, M.; Zheng, W.; Gong, Z.; Huang, P.; Li, R.; Xu, J.; Cheng, X.; Zhang, W.; Chen, X. Unraveling the Triplet Excited-State Dynamics of Bi^{3+} in Vacancy-Ordered Double Perovskite Cs_2SnCl_6 Nanocrystals. *Nano Res.* **2022**, *15*, 6422–6429. [CrossRef]
178. Das Adhikari, S.; Echeverría-Arrondo, C.; Sánchez, R.S.; Chirvony, V.S.; Martínez-Pastor, J.P.; Agouram, S.; Muñoz-Sanjosé, V.; Mora-Seró, I. White Light Emission from Lead-Free Mixed-Cation Doped Cs_2SnCl_6 Nanocrystals. *Nanoscale* **2022**, *14*, 1468–1479. [CrossRef] [PubMed]
179. Jia, X.; Wang, B.; Zhu, M.; Zhang, Y.; Chong, X.; Li, J.; Wang, J. Growth Process and Optical Properties of Cs_2ZrCl_6 Doped with Ce^{3+} and Li^+ Crystals. *Cryst. Growth Des.* **2023**, *23*, 3589–3594. [CrossRef]
180. Buryi, M.; Babin, V.; Ligthart, R.A.M.; Nagorny, S.S.; Mikhailik, V.B.; Vaněček, V.; Prouzová Prochazková, L.; Kandel, R.; Nahorna, V.V.; Wang, P. Correlation of Emission, Scintillation and Charge Trapping Properties in Cs_2HfCl_6 and Cs_2ZrCl_6 Single Crystals. *J. Mater. Chem. C* **2021**, *9*, 2955–2968. [CrossRef]
181. Vanecek, V.; Kral, R.; Paterek, J.; Babin, V.; Jary, V.; Hybler, J.; Kodama, S.; Kurosawa, S.; Yokota, Y.; Yoshikawa, A.; et al. Modified Vertical Bridgman Method: Time and Cost Effective Tool for Preparation of Cs_2HfCl_6 Single Crystals. *J. Cryst. Growth* **2020**, *533*, 125479. [CrossRef]
182. Jia, X.; Jiang, H.; Chong, X.; Ju, W.; Feng, T.; Zhao, Z.; Wei, H.; Li, J.; Cheng, S.; Wang, J. A Novel Co-Substitution Strategy for the Design, Growth, and Optoelectronic Performance Optimization of Cs_2ZrCl_6:Ce,Li Single Crystals. *J. Mater. Chem. C* **2025**, *13*, 2844–2852. [CrossRef]
183. Song, J.; Cui, Q.; Li, J.; Xu, J.; Wang, Y.; Xu, L.; Xue, J.; Dong, Y.; Tian, T.; Sun, H.; et al. Ultralarge All-Inorganic Perovskite Bulk Single Crystal for High-Performance Visible–Infrared Dual-Modal Photodetectors. *Adv. Opt. Mater.* **2017**, *5*, 1700157. [CrossRef]

Disclaimer/Publisher's Note: The statements, opinions and data contained in all publications are solely those of the individual author(s) and contributor(s) and not of MDPI and/or the editor(s). MDPI and/or the editor(s) disclaim responsibility for any injury to people or property resulting from any ideas, methods, instructions or products referred to in the content.